THE INFLUENCE OF VEGETATIVE WINDBREAKS ON FUGITIVE DUST (PM_{10}) MITIGATION AND TRANSPORT FLUX: THE ROLE OF TURBULENCE IN ENHANCING PARTICULATE DEPOSITION

by

Sean Moran

A thesis submitted to the faculty of
The University of Utah
in partial fulfillment of the requirements for the degree of

Master of Science

Department of Mechanical Engineering

The University of Utah

May 2012

The University of Utah Graduate School

STATEMENT OF THESIS APPROVAL

The thesis of _____

has been approved by the following supervisory committee members:

_____ , Chair _____
Date Approved

_____ , Member _____
Date Approved

_____ , Member _____
Date Approved

and by _____ , Chair of

the Department of _____

and by Charles A. Wight, Dean of The Graduate School.

ABSTRACT

Quantifying deposition efficiency for fugitive dust on vegetation is essential for developing more accurate computational models. This work focuses on the role that turbulent motions play in deposition enhancement. This research combines field and wind tunnel experiments to study particle deposition onto vegetation resulting from small-scale interactions of turbulent flows. These experiments will help to optimize the design of vegetative windbreaks as a mitigation tool for fugitive dust removal from the atmosphere. The long-term goal is to use these data for model development and parameterization within the Quick Urban and Industrial Complex (QUIC) dispersion modeling system. Experimental testing in a full scale wind tunnel seeks to quantify deposition efficiencies by varying the relevant Stokes number parameters (i.e., wind speed, deposition area of substrate, and particle size). Experimental results indicated that grid induced turbulence enhances deposition in all six directions (x-upstream and downstream, y-right and left, z-up and down). Deposition was enhanced on the upstream impaction surface (-x direction) by a factor of two compared to the no-grid "laminar" case. Deposition on all other directional surfaces increased by about an order of magnitude.

This work investigates the effect of isotropic turbulence on the enhancement of particle deposition to surfaces for inertial impaction dominated processes. Turbulence and particle deposition were quantified using hot-wire anemometry and fluorimetry measurement techniques, respectively. The contribution of turbulence on deposition is shown to scale with a dimensionless parameter formed from the combination of the classical Stokes number (Stk) and the Taylor-microscale Reynolds number (R_λ). This scaling helps to understand the role that the intermediate eddies (λ) and turbulent fluctuations (u') have on deposition fraction (DF_λ). A modified Stokes number ($Stk^\star$=Stk$\cdot\mathrm{R}_\lambda{}^{0.3}$) parameterization for an empirical equation (DF_λ = 100-100/(440.5$\cdot(Stk^\star)^{3.88}$+1)) was devised to utilize this new scaling and incorporate physically significant turbulent deposition parameters (i.e., λ and u') into the solution. Experimental results indicate that past impaction parameterizations substantially underestimate deposition in the presence of turbulence.

For my amazing parents and grandfather

CONTENTS

LIST OF FIGURES

LIST OF TABLES

ACKNOWLEDGMENTS

This work was sponsored by a Resource Conservation and Climate Change contract (RC-1730) through the Strategic Environmental Research and Development Program (SERDP). I would like to thank Nathan Miller for his assistance with the acquisition of hot-wire anemometry data, Tim Price and Bryan Edmunds for their assistance in collecting deposition data, Dr. Meredith Metzger for providing detailed information about hot-wire calibration and the Taylor microscale, and Dr. Leon Pahler for loaning me equipment for data collection.

I would like to thank my thesis committee for providing tremendous guidance over the course of my graduate career. Dr. Rob Stoll provided great insight into LES dispersion modeling, hot-wire data collection, and general turbulence theory that was critical in completion of this work. Dr. John Veranth helped me jump-start my graduate career and gave me full access to his lab. I am truly grateful to my advisor, Dr. Eric Pardyjak, for his constant support during my graduate career and guidance to help me develop my skills as a researcher. The knowledge and maturity I have gained from Dr. Pardyjak and the rest of my committee is unmatched.

CHAPTER 1

INTRODUCTION

The central objective of this overall research project was to develop a computational tool to optimize the use of vegetative windbreaks for controlling fugitive dust emissions as a result of wind erosion and vehicle operation on unpaved roads of military training ranges. The scope of this project is very large in that it combined three different studies: 1) Improvement of the QUIC (Quick Urban Industrial Complex) dispersion and deposition model to give a more accurate estimate for dust removal from porous media (vegetative windbreaks); 2) Validation of the deposition model using field data that examine the dust removal from porous media and 3) Conducting wind tunnel experiments to better understand how the behavior of turbulence enhances deposition. Given that this project encompasses sizable objectives, the primary focus of the research for this thesis was on using wind tunnel data to investigate the scalar interaction of dust (PM_{10}) with turbulent eddies and to develop a better parameterization to be used in future turbulent deposition models.

Deposition model development was improved by integrating wind tunnel experiments from the EFD (Environmental Fluid Dynamics) lab at the University of Utah and field data from Hanford, WA and Corvallis, OR experiments. A combination of deposition and turbulence data collected in the EFD lab are presented in the main chapter (Chapter 2) of this thesis. Field data are not presented in this thesis, but will be processed and analyzed in future papers (Speckart *et al.*) for model validation. The experimental component of the deposition and turbulence data provided new input data needed to minimize the inclusion of numerous input parameters and described dust removal as a function of the turbulent motions. This was essential in model development because it accurately described the physics of particle transport and deposition. This will create a better tool to predict potential dust emissions and fractions removed because turbulent deposition parameters are accounted for in the deposition calculations.

Chapter 2 of this thesis was submitted as a journal Letter publication in Physics of Fluids. Therefore methods and procedures could not be included in the publication and are

described in the appendices of the thesis.

1.1 Background and Motivation

Dust generated from open source mechanical disturbances of granular material is commonly known as fugitive dust because it is not discharged to the atmosphere in a confined flow stream [2]. Fugitive dust can be generated from many open sources including unpaved roads and disturbed or undisturbed land in developed and agricultural regions [3]. Emission inventories from road dust often exceed other fugitive dust sources with the exception of wind-driven erosion or aeolian dust [4]. Therefore, it is essential to mitigate these sources to comply with the regulations set be the National Ambient Air Quality Standards (NAAQS). US EPA document AP-42 [2] details emission factors for fugitive dust on paved and unpaved roads based on measurements taken at 3 m - 5 m from the roadside. However, these studies did not take into consideration the contribution that atmospheric stability and surface roughness have on particulate transport. Near source dust removal by vegetation has been shown to effectively remove fugitive dust from the atmosphere [5], but details of how dust removal rate varies with site conditions are unknown. For this reason, the deposition and transport of PM_{10} and $PM_{2.5}$ (particulate matter less than 10 μm and 2.5 μm - aerodynamic diameter, respectively) onto vegetation is the primary focus of this research project. Particles in this size range can be generated from vehicular activities on unpaved roads and can degrade local and regional visibility, as well as contribute to adverse cardiovascular and respiratory effects [6, 7, 4, 8].

Deposition of dry particles in the atmospheric boundary layer is governed by the turbulent flow characteristics, the physical and chemical properties of the material being deposited, and the nature of the surface [6]. As a vehicle travels on an unpaved road with near source vegetation, the force and rotation of the wheels generate mixing of the granular surface materials that suspend the dust particles [2]. The rotation of the wheels as well as the interaction of turbulent shear with the surface causes the suspended particles to move with the turbulent wake behind the vehicle. The turbulent motions of the particles are advected and deposited into the vegetative canopy by the bulk turbulent motions and the mean wind. The working hypothesis behind this research is that these turbulent motions enhance particulate deposition on all surfaces, even for the smaller particles that do not typically deposit. In effect, impaction is not only playing a role on the upstream surfaces [9, 1], but on all other surfaces as well. A field experiment that supports this hypothesis measured deposition on artificial vegetation for all axes [10]. Prior field data from our

research group suggested that there was significant dust removal [11, 12, 13] and enhanced deposition of PM_{10} due to the interaction of the turbulent vehicle wake with solid surfaces [14]. However, the cost and variability of field studies made it difficult to precisely quantify this effect.

In a study on pesticide spray drift, [15] emissions were reduced by as much as 90% when a windbreak was used over a homogenous surface. In two separate published field studies by this research group at U.S. Army Dugway Proving Ground, UT [12] and Ft. Bliss, TX [11], the mass fractions of initial dust removed were ∼85% and ∼9.5%, respectively. Large shipping containers were used to simulate an urban type setting at Dugway Proving Ground and sparse vegetation was used at the Ft. Bliss site. Analytic models were also tested for both field studies with varying atmospheric conditions and terrain irregularities. The differences in results with various atmospheric stabilities and surface roughness elements reported from both authors, as well as results from other studies [16, 17, 18, 6, 4], points toward a greater need for future experiments that will help give better input parameters for deposition model estimates. With improved input parameters deposition models can better predict dust removal from windbreaks in hopes of improving air quality.

Controlling fugitive dust is particularly important in populated arid regions where a larger populace prone to respiratory illnesses could be exposed. This also becomes a local problem when urban development is established close to a military base. Conventional dust mitigation strategies such as chemical spraying and watering are not economically practical on military training facilities given the long miles of unpaved roads that exist. The most likely and feasible strategy for reducing these emissions would be accomplished in the utilization of natural vegetation and windbreaks [6, 4, 13, 12]. Controlling particulate transport using windbreaks is not only important in improving air quality, it has many important agricultural applications as well (fungal and spore dispersion, erosion, genetic contamination of different plant species, pesticide spray-drift, etc.). Windbreaks consisting of vegetative canopies [13], terrain irregularities [19], and fences [20] have been shown to significantly reduce particulate emission in the atmosphere. For the purpose of this research project, windbreaks consisting of vegetative canopies are used to provide significant near-source mitigation of vehicle-generated fugitive dust. Field studies from this group along the US-Mexico border have demonstrated that benefits of vegetative windbreaks exist even with low-growing arid climate species such as mesquite [13]. The relative height of the canopy and the initial dust cloud is the most important parameter characterizing dust deposition [5]. Prior work has shown that ground-level wind patterns and atmospheric stability also

influence the partitioning of initially suspended dust between long-range transport and near-source deposition [4, 5].

As previously stated, in order to accurately quantify the deposition fraction removed by vegetative surfaces, models must implement the underlying physical mechanism (i.e., eddy-particle interaction) for deposition. Three widely known models for deposition in vegetative canopies [18, 17, 16] that use different assumptions and input parameters have demonstrated the influence of vegetation on deposition. However, their low estimates on deposition fraction removed by the vegetation raise some question as more recent studies have reported a need for more parameterization [12, 5, 21, 6] to account for these discrepancies. Studies on deposition in pipe bends [22, 23, 24] or straight ducts [25] have shown the influence of turbulence on deposition. However, very limited model development has sought to account for the eddy-particle deposition interaction [23, 26] and no current experimental studies have investigated this physical interaction of turbulent eddies with the particles responsible for deposition in a vegetative canopy. The study in this paper seeks to bridge the gap between particle deposition and the eddy-particle interaction in vegetative canopies. This will be accomplished by using the results from a wind tunnel study to improve estimates in the existing QUIC Dispersion Modeling System.

1.2 Field Experiments

There were two field studies partially funded by this research project (Strategic Environmental Research and Development Program) that aimed to validate future models: 1) Fugitive dust dispersion and deposition using native vegetation for dust control at Pacific Northwest National Lab (PNNL), Hanford, WA from June 6, 2011 to June 13, 2011 and 2) Particle transport in a vineyard canopy to investigate spore dispersion and growth in Corvallis, OR from September 26, 2011 through October 4, 2011. The campaign conducted at PNNL used vehicular traffic from a large van and truck to generate fugitive dust. A sufficient amount of time was allotted (between vehicle passes) for the dust cloud to advect past the monitoring equipment before the next vehicle pass was made. The objectives for this study were to verify the ability for QUIC to estimate PM_{10} transport and deposition given certain input parameters (i.e., leaf area index and atmospheric stability) and to better understand the behavior of PM_{10} with in a vegetative canopy. Optical sensing devices (TSI, DustTrak 8520) were used to measure PM_{10}. The Corvallis campaign was performed in collaboration with Dr. Walt Mahaffee from the Agricultural Research Service of the USDA and Dr. Rob Stoll from the Mechanical Engineering Department at the University of Utah.

The objective of this study was to correlate these deposition results with those observed in the wind tunnel using similar particle sizes (d_p = 1-5 μm) but different turbulence intensities. An aerosol generator released the small fluorescent particles into the fully foliated vineyard at several heights. Particles were deposited onto small rotorod impaction cylinders and taken to the lab for concentration measurements. Sonic anemometers were used in both studies to acquire turbulence data.

1.3 Dispersion and Deposition Modeling

Many researchers are interested in how particles are transported in the atmosphere by the turbulent wind field and then deposited. For dispersion models there are two types of reference frames used to represent the particle motion: 1) Eulerian and 2) Lagrangian. Eulerian models track the particle motions in and out of a fixed grid and Lagrangian models track the trajectories of individual particles. The complexity and computational time required for Lagrangian models is significantly more. However the results are generally more accurate for complex turbulent flows. For both dispersion models, particles transported in and out of the vegetative canopy can be represented by the mean advection and turbulent motions of the atmosphere.

For modeling the deposition of particles there are two common approaches that are used in a vegetative canopy: 1) Horizontal advection scheme and 2) Vertical resistance scheme. The horizontal advection scheme models the turbulence statistics and parameterizes the mean velocities and concentrations to account for windspeed, atmospheric stability, vegetation height, etc. This scheme has become relatively common in deposition models for plant canopies [17, 18, 5]. The idea of the horizontal advection scheme is to represent the particle deposition by a combination of a deposition velocity term (v_d) and gravitational settling term (v_s). The deposition velocity generally incorporates inertial impaction, Brownian diffusion, and interception. The way in which these terms are calculated vary from author to author [17, 18, 5]. However they all incorporate an impaction and gravitational settling term. The vertical resistance scheme for dry particles (different for gaseous species) equates the deposition velocity (v_d) to the sum of three resistances in series and one in parallel: the turbulent motions governing particle transport across the surface layer (r_a), particle transport across the quasi laminar layer from molecular diffusion (r_b), and the particle settling velocity (v_s). The deposition velocity (v_d) and this resistive network analysis are commonly used as a an estimate for deposition in well known models [16].

$$v_d = \frac{1}{r_a + r_b + r_a r_b v_s} + v_s \tag{1.1}$$

The particle transport across the surface layer and the quasi laminar layer account for the windspeed, vegetation height, leaf size, and atmospheric stability [27]. From Eq. 1.1, the surface layer (r_a) turbulent transport is the driving mechanism that brings the particle down to the surface. Values of r_a can be determined from micrometeorological measurements and surface characteristics (i.e., windspeed, temperature, radiation, and surface roughness length) [27] Particle impaction across the quasi laminar layer (r_b) considers Brownian diffusion, inertial impaction, and interception as possible mechanisms for deposition. There exists a canopy resistance (r_c) term that is excluded from this estimate because r_c is equal to zero when particle rebound is negligible. Deposition by gravitational settling is described in v_s and is more prevalent in larger particle sizes since v_s increases as the square of the particle diameter. Complete expressions for r_a, r_b, and v_s are laid out in Seinfeld and Pandis [27].

Regardless of the deposition scheme implemented in the dispersion models, the novel parameterization presented in this paper can be applied to either approach and offer the same model improvements (i.e., enhanced deposition) because both consider inertial impaction as a deposition mechanism. This is important because the turbulent deposition results from this paper only consider data from the inertial impaction surface in the parameterization for future models. (The parameterization from wind tunnel experiments will be discussed shortly.)

1.4 Wind Tunnel Experiments

A large majority of deposition models in the existing literature [18, 17, 16, 5, 28] are derived using empirically fit data from wind tunnel studies developed by May and Clifford [9]. These studies by May and Clifford [9] tested the impaction efficiency of four different idealized surfaces (i.e., ribbons, cylinders, spheres, and discs) using 20-40μm diameter particles at varying wind speeds. This paper recognizes a fundamental problem with using these data because these experiments were conducted under well-mixed laminar flow conditions. Problems posed for deposition models in the atmosphere are extremely turbulent and this turbulent behavior is known to generate more particle mixing, thereby enhancing deposition to vegetative surfaces [12, 11]. Therefore, it seems reasonable to hypothesize that deposition models empirically fit to an equation from laminar flow experiments will under predict deposition every time.

To improve model estimates for deposition to vegetation and account for the turbulent nature in the atmosphere as well as the enhanced mixing behavior within vegetative canopies, turbulent deposition experiments were conducted in a full scale wind tunnel at the University of Utah. Deposition measurements were recorded separately from the turbulence measurements. Deposition results from this paper attempt to give a new empirical fit for parameterizing deposition models and improving deposition estimates in the presence of turbulence.

1.4.1 Deposition Measurements

Deposition of particles onto known surfaces is governed by multiple deposition mechanisms: Inertial impaction, gravitational settling (or sedimentation), Brownian diffusion, interception, and phoretic precipitation. The most predominant mechanism for particles in approximately 1-20 μm diameter range is inertial impaction. Larger particle diameters (>20) are deposited by gravitational settling and inertial impaction. Both impaction and gravitational settling are results of particles crossing streamlines because the inertial forces of the particle are greater than the viscous forces. Brownian diffusion is associated with the deposition of smaller particles (submicron level) and results from the collision of particles with the air molecules. Interception occurs when the particle diameter is large compared to the distance to the surface which it is impacting. Phoretic precipitation is a result of particle motion dominated by large gradients (i.e., isotropic turbulence to inhomogenous turbulence).

Deposition measurements taken from the wind tunnel study had a particle diameter range of 0.54-9.00 μm and a mean diameter of 3.43 μm. Deposition was dominated by inertial impaction due to the particle size distribution. Nonvolatile liquid particles (400 mL of distilled water, 100 mL of glycerol, and 0.25 g of fluorescein) were injected upstream of the turbulence grid and deposited onto smooth square plastic substrates. For all wind tunnel deposition experiments a standard, right hand coordinate system was used for direction reference (when looking downstream of the wind tunnel). The +x direction referred to the downwind surface perpendicular to the streamwise flow and the +z direction was vertically facing surface parallel to the streamwise flow. A detailed explanation of these experiments is discussed in Appendix A.

1.4.2 Turbulence Measurements

A turbulence grid was placed at the entrance (throat) of the converging test section to generate isotropic, homogenous turbulence. Since this type of flow has been studied

extensively both experimentally [29, 30] and theoretically [31, 32], it provides an ideal experimental framework for relating various scales of turbulence to deposition characteristics. Furthermore, this type of turbulence was desired because it is believed that turbulence within the canopy is more homogenous due to the turbulence interaction with the vegetation in the canopy. The turbulence grid used for this study was machined from 2.54 cm, square acrylic rods. They were fashioned together both vertically and horizontally so a grid solidity of 50% was achieved. To quantify the effects of turbulence on deposition a hot wire probe was placed at the locations where deposition measurements were recorded. The particle interaction with the Taylor-microscale (λ) was of most importance in this paper and is discussed in further detail in Chapter 2. A detailed explanation of the turbulence experiments is discussed in Appendix B.

CHAPTER 2

DEPOSITION ENHANCEMENT AND TURBULENT MOTIONS

A workshop conducted by the Desert Research Institute (DRI) [4], as well as recent observations from field experiments [33, 12], reported near source deposition enhancement via the interaction of PM_{10} (particles with an aerodynamic diameter $\leq 10\mu$m) with vegetative surfaces in the atmosphere. A conceptual model [6] was developed from this workshop to account for the systematic under-prediction of PM_{10} deposition to vegetation, in the presence of turbulence. Other recent deposition models [23, 26] have attempted to incorporate bulk boundary layer effects of turbulence into their models without focusing on the interaction of particles with individual elements. In addition, turbulent deposition experiments from flow through pipe bends [22] and channels [25] have sought to understand the effects of turbulent motions on deposition. Although these experiments and models have improved turbulent deposition results, they suggest a critical need to better understand the fundamental physical interaction between particles and vegetative elements in addition to the deposition mechanisms used to capture these interactions. We hypothesize that a turbulence deposition parameter should be included in the impaction mechanism to capture the complex physical interaction between the turbulent mixing of particles and the surfaces to which they deposit. The omission of such a parameter is hypothesized to be an important source of error in current deposition models for vegetative canopies [5, 17, 18], where they are formulated from laminar flow impaction theory [1] and experiments [9, 34] in which particles deposit to idealized surfaces (further referred to as substrates).

Typically, the turbulent Reynolds number used to characterize the motion in grid-generated turbulence is represented by the Taylor-microscale Reynolds number ($R_\lambda \equiv u'\lambda/\nu$, where u' is the r.m.s. of the streamwise velocity, λ is the Taylor microscale, and ν is the kinematic viscosity of the fluid). The Taylor microscale is defined for isotropic turbulence as $\lambda = [\langle u'^2 \rangle / \langle (\partial u'/\partial x)^2 \rangle]^{1/2}$, where the angle brackets denote averaging and λ represents the intermediate eddy-size between the integral length scale of the grid mesh (M$\approx$ 0.086 m) and

the smallest size eddies responsible for dissipation of energy [31] (Kolmogorov length scale, η). Physically, λ describes the average distance it takes for the turbulent fluctuations (u') to rapidly increase or decrease across two standard deviations in magnitude. The relative size of λ is shown in Fig. 2.1.

This paper examines a turbulent scaling parameter R_λ that can be used to describe the physics of the flow as particles interact with the turbulent eddies (λ) believed to be most prevalent in deposition. A turbulence grid with a mesh-bar width ratio of 50% was used to generate isotropic turbulence. Turbulent measurements were then collected so that the scales of turbulence (λ) in the wind tunnel could be correlated with our deposition results. The isotropic turbulent deposition data were compared with data from laminar flow experiments to investigate the impact of turbulence.

As described in a recent communication by the author [35], a fluorescein (0.5 mg/mL), glycerol (20%), and distilled water (80%) solution was aerosolized from an ultrasonic humidifier (Model V5100NS, Kaz Inc., Hudson, NY) and injected from a point source at the upstream convergent section of a wind tunnel. The test section length was 2.5 m and the cross-section was 1.22 m by 0.61 m. Within the test section particles were deposited onto square, smooth plastic substrates (hard polypropylene). The substrates were fixed in the center of a six-axis deposition frame in the wind tunnel and suspended by 24-gauge aluminum wire. The frame was placed at two different distances (x) downstream of the grid (1.80 and 2.13 m) during the experiments. The substrates were then held together on the wires using a pressure-sensitive adhesive (Blu-Tack, Bostik, Paris, FR). Deposition experiments required a laser-based particle spectrometer (Grimm 1.109, Grimm Technologies Inc., Douglasville, GA) to measure the concentration of aerosol particles with a mean diameter of 3.43 μm and bimodal distribution between 0.54-9.0 μm. The experimental results were described by the deposition fraction (DF) of aerosol particles that deposited onto all six axes ($\pm$x,$\pm$y,and $\pm$z) and were quantified using Eq. (2.1):

$$DF(\%) = \frac{\text{Mass deposited}}{\text{Mass in airstream}} \times 100\% = \frac{M_w}{U\ A\ t\ C_m} \times 100. \tag{2.1}$$

Here, we assumed that the nonvolatile liquid aerosol particles stuck to the substrate upon contact and there was no particle rebound. Deposition of the fluorescein/glycerol particle to the substrates were determined using a Fluorimeter (1420 Victor3V, PerkinElmer Inc., Waltham, MA) from a fluorimetry measurement technique. DF was calculated using the

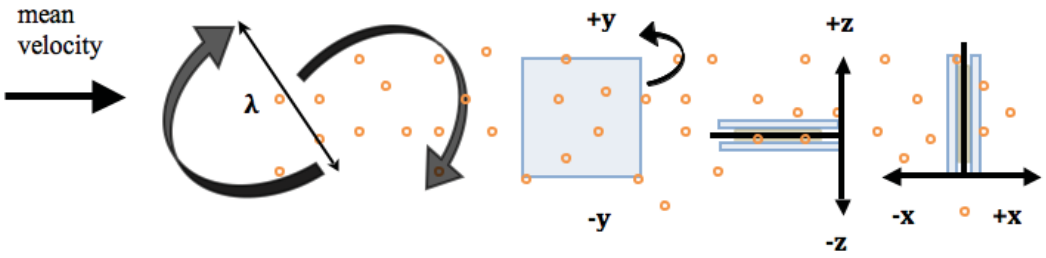

Figure 2.1. Schematic showing the eddy-particle interaction as they advect downwind and deposit to the six substrate axes.

mass of the deposited fluorescein M, the mean streamwise velocity U, the area of the substrate A, the total run-time of the experiment t, and the local aerosol concentration C_m. DF is defined as the fraction of deposited aerosol particles flowing in the path of the substrate. The important role that turbulent mixing has on increasing particle deposition to all surfaces is illustrated in Table 2.1 where DF is noticeably enhanced (on all axes) by the grid. Our results differ from prior deposition studies of laminar [9, 17] and turbulent [22] flows which suggested that inertial impaction on the frontal surfaces ($-x$) and gravitational settling on the vertically facing surfaces ($+z$) only warranted attention.

However, our grid-generated turbulence experiments at U= 4.84 ms^{-1} revealed that deposition (all six axes combined) was enhanced by approximately 250% in comparison to our no-grid experiments at the same mean velocity. The most significant increase in deposition between the laminar and turbulent experiments occurred on the nonimpaction surfaces where the turbulent fluctuations and the scales associated with them actively transported and deposited the aerosol particles. The isotropic behavior of grid turbulence enabled the turbulent eddies to transport the particles more uniformly onto all axes, thereby significantly enhancing deposition. At higher velocities (U at 4.84 and 8.06 ms^{-1}), inertial impaction on the frontal surface ($-x$) was the dominant deposition mechanism due to the bulk advection of particles being transported and deposited by the mean streamwise velocity. Deposition at lowest velocity (U = 1.65 ms^{-1}) showed clear evidence that inertial impaction on the frontal surface ($-x$) was no longer dominated by the mean streamwise velocity. Instead, the isotropic nature of the turbulence contributed to depositing particles onto all surfaces more equally, as shown in Table 2.1. Furthermore, these data for 3.43 μm particles indicated gravitational settling was not a dominating mechanism for deposition. With larger diameter particles $\gtrsim$ 20 μm, gravitational settling would certainly be more of a prevalent deposition mechanism because the effective terminal settling velocity increases as the square of the particle diameter. Nonetheless, our results imply that certain scales of turbulence assist in enhancing deposition to surfaces and that these scales should be accounted for within the deposition parameter.

The Stokes number (Stk) is the governing parameter typically used to quantify deposition efficiency by inertial impaction onto a given surface. Based on the advection of a fluid particle, it is the ratio of the particle stopping distance in the free-stream velocity to characteristic length of the obstacle, [1] which is given by Eq. (2.2):

$$Stk = \frac{\rho_p \, d_p^2 \, C_c \, U}{18 \, \mu \, L_s}. \tag{2.2}$$

Table 2.1. $DF(\%)$ on all six substrate axes are shown for grid and no-grid generated turbulence. The substrate lengthscale (L_s) was 1 cm and deposition results were all acquired at 1.8 m from the entrance of the convergent section of the wind tunnel . The error bars refer to the uncertainty from the error propagation in calculating Stk and DF.

	U= 1.65 ms^{-1}	U= 4.84 ms^{-1}	U= 8.06 ms^{-1}	U= 4.84 ms^{-1}
Axis	grid $DF(\%) \pm$ err	grid $DF(\%) \pm$ err	grid $DF(\%) \pm$ err	no-grid $DF(\%) \pm$ err
$-x$	5.7 ± 1.8	11.8 ± 1.5	31.2 ± 2.6	6.8 ± 0.7
$+x$	3.8 ± 1.7	4.3 ± 1.5	3.0 ± 1.3	0.5 ± 0.2
$-y$	4.1 ± 1.8	4.7 ± 1.4	4.0 ± 1.4	0.8 ± 0.3
$+y$	4.6 ± 1.7	4.6 ± 1.5	4.2 ± 1.2	0.6 ± 0.2
$-z$	4.3 ± 1.9	4.2 ± 1.2	4.4 ± 1.4	0.8 ± 0.2
$+z$	4.1 ± 1.7	3.7 ± 1.1	4.3 ± 1.3	0.6 ± 0.2

Stk in Eq. (2.2) depends on the density of the spherical particle ρ_p, the particle diameter d_p^2, the Cunningham correction factor C_c ($\sim$1 for mean free paths $\ll$ particle diameter), the mean free-stream velocity U, the dynamic viscosity of the fluid μ, and the substrate lengthscale L_s. Although Stk only describes deposition from inertial impaction, it is used in almost all deposition models because inertial impaction has the greatest influence on deposition for a wide range of problems. Stk for our experiments were varied using three U values (1.65, 4.84, and 8.06 ms^{-1}) and three L_s values (0.5, 1.0, and 1.4 cm) to achieve a wide range of Stk values. Marple and Lui (1974) used exact numerical simulations of the Navier-Stokes equations (for a known particle sizes and laminar flow) to compute deposition fraction as a function of Stk for various particle sizes, and produced a characteristic "S-shaped" impaction curve. May and Clifford's (1967) laminar flow deposition results onto geometric surfaces were similar to Marple and Lui's theoretical curve. However, they observed much larger ranges of Stk ($0.1 \leq Stk \leq 100$). The results of May and Clifford have been used to develop a widely accepted deposition parameterization for impaction [18, 17] ($DF = Stk/(Stk+f_p)^2$ where f_p ($0.4 \leq f_p \leq 0.9$) [9]) onto similar geometric shapes (e.g., vegetative surfaces). In theory, these results could be extended for similar impactor geometries operating at similar Reynolds numbers and Stk. However, our data in Fig. 2.2 present a different explanation to that theory. The effect of turbulence on particle deposition appears to be systematically shifted toward a lower range of Stk ($0.01 \leq Stk \leq 0.1$). Based on the theoretical deposition curve of Marple and Lui [1] and our observed Stk, we would expect to detect almost no deposition onto the impaction surfaces. Instead our data covered almost all ranges ($0 < DF \leq 100$) of DF at significantly lower Stk. We attribute this increase in deposition at lower Stk to the turbulence intensity ($u_i = u'/U$) generated by the grid and the interaction of the associated scales with the substrate. For sufficiently large turbulence intensity ($\gtrsim$4%), momentum is transferred to the particles, resulting in an enhanced ability to deposit. The fluctuations generated by the grid add a turbulent deposition mechanism analogous to Brownian diffusion, but at a much larger scale. This turbulent deposition component is neglected in current models and as a result, Stk alone fails to describe the enhanced deposition observed in turbulent flow. Note that the largest error source in calculating Stk was due to the large distribution of particle sizes produced from the ultrasonic humidifier. The x-axis error bars on the left side have been negated for clarity.

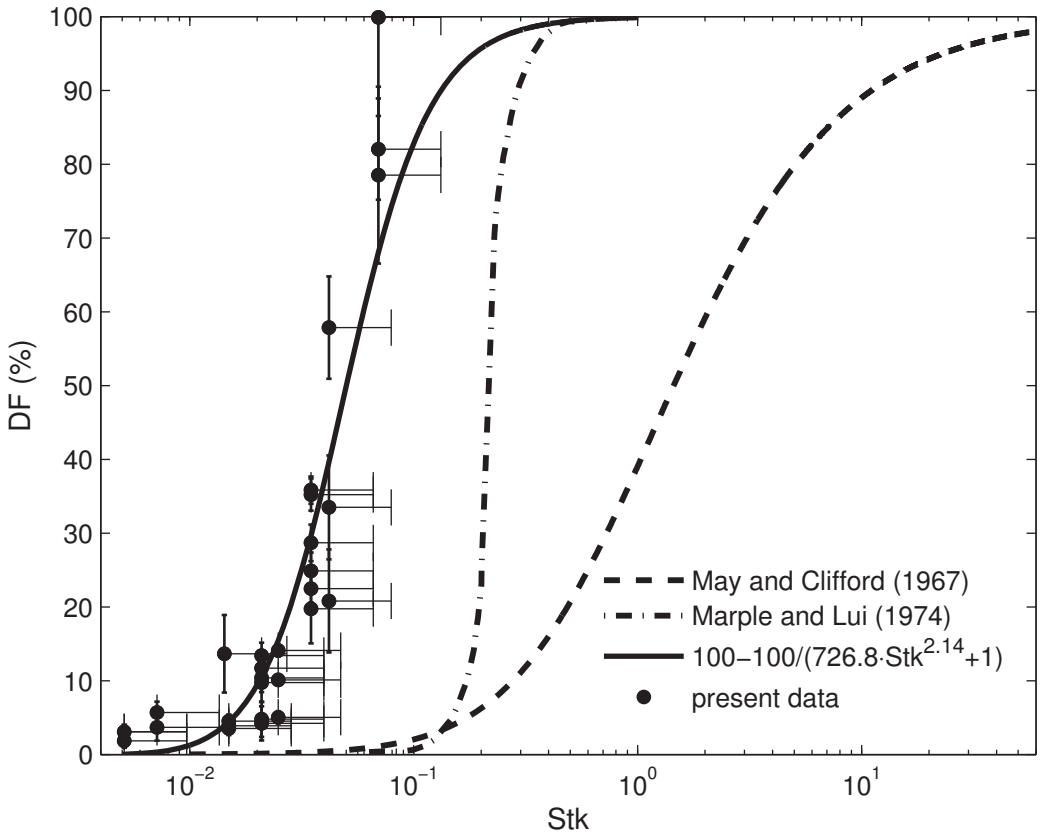

Figure 2.2. Deposition results of our present data (•), a least square fit to our data (–), Marple and Lui (1974) (–·–), and May and Clifford 1967 (– –). The error bars refer to the uncertainty from the error prorogation in calculating Stk and DF. The largest error sources are due to the distribution of particle sizes and the concentration measurements.

2.1 Scaling by R_λ

To better understand the effects of turbulence and to compute R_λ, we placed a single-sensor hot-wire probe (55P16, Dantec Dynamic, Denmark) in the wind tunnel to measure u' and λ. Values of R_λ were determined by varying the mean speed of the air in the wind tunnel ($1.5\ ms^{-1} < U < 8.5\ ms^{-1}$). From the raw hot-wire data, a power law relationship developed from King's law was used to calibrate the wind tunnel velocity measurements [36]. These data were used to calculate the deposition dependent scales of turbulence λ in the wind tunnel. This was accomplished by fitting a parabolic polynomial regression to the first three points at the origin of the familiar autocorrelation function[32, 31]: $\rho(s)=\langle u'(t)u'(t+s)\rangle/\langle u'(t)^2\rangle$, where $u'(t)$ is the fluctuating velocity component at time t and $u'(t+s)$ is the fluctuating velocity component at a time lag of $t+s$. The fitted parabola at the origin $\rho(s)$ gives a time scale relation when it crosses the x-axis of the autocorrelation. To determine the length scale λ the time scale was multiplied by the local mean advection velocity (U) assuming Taylor's frozen turbulence[32, 31]. We hypothesize that λ is the appropriate turbulence length scale to characterize deposition onto known surfaces because this length scale is shown to have the smallest dynamic eddies [32], which should be most responsible for turbulence enhanced deposition. Dimensional analysis using the Buckingham Pi theorem indicates that impaction-dominated DF depends on twelve variables: $DF =$ f(U, ρ, d_p, u', λ, L_s, ρ_p, μ, D, x, M, g), where D is the mass diffusion coefficient and g is the acceleration of the particle due to gravity. The three dependent variables chosen for analysis were the mean streamwise velocity U, the density of the air ρ, and the mean diameter of the aerosol particles d_p. The functional dependence of the dimensional variables was reduced in terms of nine independent nondimensional terms. The relevant contribution to DF was considered for every combination of dimensionless terms and their importance could be reduced to two dimensionless terms, Stk and R_λ. Therefore, we can conclude that λ is a relevant length scale for deposition. At these smaller scales the eddy-sizes of λ are expected to interact with the aerosol particles and have the most substantial contribution in actively depositing these particles onto the substrate surfaces. Fig. 2.1 gives an appropriate visual representation of how we hypothesize λ interacts with the aerosol particles to enhance deposition onto our substrates.

The deposition results shown in Fig. 2.2 suggest a turbulent Reynolds number effect on deposition. Specifically, the turbulent flow data follow the theoretical curve presented by Marple and Lui (1974) for laminar flow [1], but are shifted toward smaller Stk. Given the functional dependence that Stk and R_λ have on DF, an empirical turbulent Reynolds

number scaling was used for our data by performing a least squares minimization technique between our data and that of Marple and Lui. When Stk was scaled by $R_\lambda{}^{0.3}$, error was minimized and this scaled correction collapsed our data onto the theoretical curve from Marple and Lui quite well, as shown in Fig. 2.3. The scaling of $Stk{\cdot}R_\lambda^{0.3}$ created a new modified Stokes number $Stk^\star$. A least square function given in Eq. (2.3) was fit to our modified turbulent deposition data to develop a curve that compared well with the theoretical curve in Marple and Lui for inertial impaction under laminar flow conditions.

$$DF_\lambda = 100 - \frac{100}{440.5(Stk^\star)^{3.88}+1}. \tag{2.3}$$

The resulting curve and the laminar flow curve shown in Fig. 2.3 have very similar DF values. However, there were some differences at the lower and upper limits of DF. A maximum difference ($\sim$25%) in Stk between the two curves was observed at a DF of $\sim$4%. The deposition data corresponding to $U \sim 1.6$ ms^{-1} were excluded from the fit because for $R_\lambda \leq 50$, turbulence is considered very weak and not well-defined [29]. R_λ measured at $U \sim 1.6$ ms^{-1} were in a range of $40 \leq R_\lambda \leq 43$ and were not in the fully turbulent range necessary for this scaling. All deposition results presented in the fitted equation displayed strong turbulence behavior ($R_\lambda \geq 200$) which gave rise to larger turbulent fluctuations that drove the length scale λ, most responsible for enhanced turbulent deposition. In Fig. 2.3 it is apparent that our scaled experimental results and empirical parameterization, which include the effects of turbulent deposition, closely resemble the numerical, laminar results from Marple and Lui. Due to the collapse of the $Stk^\star$ curve onto the Stk curve, the modified Stokes number ($Stk^\star$) provides for a physical explanation analogous to the classical interpretation of the Stokes number (Stk) (i.e., for $Stk \gg 1$ particle deposition is extremely likely ($\sim$100%) while particle deposition is less likely for $Stk < 1$).

To conclude, the results presented in this Letter have shown that turbulence certainly enhances deposition on all surfaces. For problems where impaction dominates turbulent deposition, a modified Stokes number $Stk^\star = Stk{\cdot}R_\lambda^{0.3}$ was proposed to account for the turbulent eddies interacting with the particles. This collapsed the turbulent deposition results onto the classical Marple and Liu Stk curve. Eq. (2.3) was developed to improve current and future deposition models that under-predict deposition due to the absent dynamics of the turbulent eddies. Fig. 2.3 shows that for fully turbulent flows ($R_\lambda \geq 50$) with geometric surfaces similar to our experiments, deposition can be enhanced by the

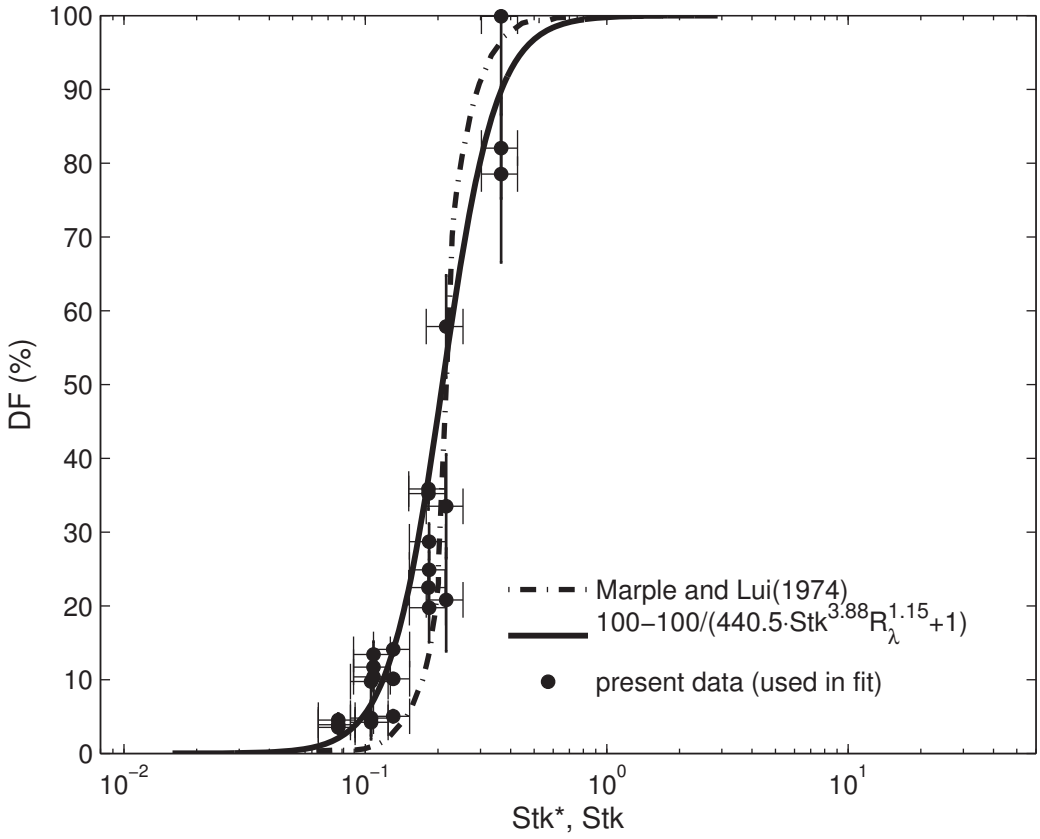

Figure 2.3. DF_λ is plotted for both classical Stokes number Stk and modified Stokes number $Stk^\star$ where $Stk^\star = Stk \cdot \mathrm{R}_\lambda^{0.3}$ for $\mathrm{R}_\lambda \geq 50$. The error bars refer to the uncertainty from the error prorogation in calculating Stk and DF.

contribution of the turbulent fluctuations u' and its associated turbulent lengthscale λ. The modified turbulent $Stk^{\star}$ provides a framework that can be considered in future, more complex experiments and offers a physical interpretation of the impaction parameter (DF_{λ}) in the presence of isotropic turbulence. Furthermore, our wind tunnel experiments help validate observations [33, 12, 4] pertaining to the interaction of turbulent motions with PM_{10} and the vegetative canopy significantly increased deposition. This empirical evidence points towards a possible change in how turbulent deposition models should quantify deposition.

CHAPTER 3

CONCLUSIONS

A number of deposition experiments were conducted with grid generated turbulence at the University of Utah's Environmental Fluid Dynamics laboratory. Data were taken using mean velocities (U) of 1.65, 4.84, and 8.06 ms^{-1}, substrate lengths (L_s) of 0.5, 1.0, and 1.4 cm, and deposition locations (x) at 1.80 and 2.13 m from the turbulence grid. No-grid turbulence experiments were also conducted using a U = 4.84 ms^{-1}, L_s = 1.0 cm, and x = 1.80 m to compare a more "laminar" type deposition experiment. Three key findings resulted from these experiments:

1. Total deposition fraction (DF) of PM_{10} was enhanced by ~250% on all six axes from the turbulent eddies created from the grid (compared to the no grid results). Deposition was improved by approximately twice as much on the frontal impaction surface ($-x$) and almost an order of magnitude on all other axes. Deposition due to gravitational settling had no effect because the particle size range (0.54-9.00 μm) was relatively small for sedimentation to be an important factor in deposition.

2. DF was nearly isotropic at 1.65 ms^{-1} because deposition from impaction was not dominated by the advection of the particles from the mean flow. Rather, the isotropic turbulence governed deposition. There appears to be a limit for deposition onto the nonimpaction surfaces ($+x$,$\pm y$,$\pm z$) at velocities of 4.84 ms^{-1} and 8.06 ms^{-1}. However, deposition on the frontal impaction surface only improves as the velocity increases.

3. For turbulent deposition an empirical equation (Eq. 2.3) was developed to improve current and future turbulence models where inertial impaction is the dominant deposition mechanism. This empirical equation was fit to theoretical results from Marple and Lui [1] by scaling the Stokes number Stk by the Taylor-microscale Reynolds number R_λ. A least squares error minimization technique was used and determined that $R_\lambda{}^{0.3}$ was the best fit to the Marple and Lui data.

Although all result findings are very important for understanding the influence turbulent eddies have on deposition, finding 3) is key to this paper. Previous deposition schemes [18, 17, 5, 21] that used May and Clifford's [9] empirical equation (from the "laminar" wind tunnel data for inertial impaction to idealized geometric surfaces) can input this new impaction parameter into their model using Eq. 2.3 to improve their estimates for DF. This parameter captures the physical interaction between the turbulent eddies and the particles to enhance deposition. The turbulent fluctuations (u'), related to the Taylor-microscale (λ), transfer momentum to the particles [37] and improve their ability to deposit. The relation of turbulence enhanced deposition to λ and to u', which transfers momentum to the particles, is essential to support and understand the hypothesis; certain scales of turbulence act to enhance deposition to vegetative surfaces. The implication of these results from this paper could not only influence local deposition model results, but they could also be used for a broader range of regional scale air quality models

A detailed uncertainty analysis was performed for all experimental procedures as outlined in Mechanical Measurement [38]. The uncertainty analysis consisted of precision uncertainty from four different measurements: the scatter in concentration measurements, the range of particle size distribution, variability in deposition measurements from experiment to experiment, and the deviations in velocity measurements. The propagation of uncertainty in these measurements is accounted for in the error bars of the DF results.

3.1 Future Work

Although the field study results from Hanford, WA and Corvallis, OR are not detailed in this paper, future analysis will be performed by this research group to validate the models that use the new parameterization developed from the work in this paper. The little work that has been accomplished on the Hanford, WA data has shown that the QUIC model accurately predicts dust removal up to ~100 m from the source. Given certain input parameters (i.e., wind direction at four heights, friction velocity, wind speed, atmospheric stability, canopy height, leaf area index) the QUIC model gives near source dust removal estimates, which highlight the mitigation benefits windbreaks can offer.

3.1.1 Model Implementation

Integrating Eq. 2.3 into QUIC is the next step of this research project. The new deposition results from QUIC will be compared with the field study results described above. QUIC's current capabilities include modeling the dispersion [39, 40] and deposition [41] of PM_{10} in vegetative canopies. The work of Cionco [39] and Judd [40] in conjunction with a

mixing length turbulence model give good approximations for dispersion within a canopy. However, the Amatul [41] deposition model only gives relative estimates of PM_{10} deposition within the canopy. The new parameterization should improve deposition estimates when implemented into QUIC.

Selecting the appropriate turbulence length scale will be up to the discretion of the modeler. For example, LES (Large Eddy Simulation) filters out everything from the integral length scale (I) down to the Kolmogorov length scale (η). Therefore, a model would have to be used to resolve these scales or a different length scale must be applied (instead of λ). Also, a friction velocity ($u_\star$) might be a better choice for deposition estimates in atmospheric boundary layer problems instead of u'. With new length and velocity scales used a new atmospheric turbulent Reynolds number will be developed.

3.1.2 Deposition Experiments

Thus far, deposition experiments have been tested on idealized plastic substrates to simulate real vegetation. Further experimental work is needed to get a better idea for how windbreaks should be implemented along roadways. Future work to be performed in the wind tunnel will focus on sheltering effects of deposition, understanding the positive or negative effects of leaf flutter on deposition, varying the surface roughnesses of the substrates, using a fractal tree to measure total deposition, using real and artificial vegetation to see how they relate to deposition results from this paper (with plastic substrates), and using larger particles (10-20 μm) to see if there are any different regions of DF vs Stk. It is believed that there is more than just one regime of turbulent DF, like the one seen in Fig. 2.2, for larger particles. This may explain why the literature is sparse for turbulent deposition results with smaller particles (PM_{10}). Deposition experiments using larger particles will give more insight into the turbulent interactions with these particles that deposit to the vegetation.

A few modifications to the turbulence grid placement and design are suggested for future improvements to the turbulent deposition experiments. Grid generated turbulence studies [30, 29] have shown that isotropy was improved when a turbulence grid was placed upstream of the contraction in the wind tunnel. With this grid placement the turbulent energy levels changed (i.e., isotropic) downstream of the grid due to the directional vortex distortions at the contraction [30]. Active grid generated turbulence have also been shown to improve the isotropic behavior in the wind tunnel [29]. In an active grid, motors rotate vertical and horizontal rods that are connected to winglets. These winglets add turbulent kinetic energy to the flow and improve the isotropic motions coming off of the grid. An active grid placed

at the upstream of the converging section in the wind tunnel would be the optimal choice for future studies. A final suggestion to improve isotropy within the wind tunnel would be to design or modify the supports which hold the turbulence grid in place (discussed in Appendix B). This would likely improve the isotropy of the turbulent flows inside of the wind tunnel and it is a quicker improvement. Regardless of the grid improvements discussed, new hotwire measurements would be required.

APPENDIX A

DEPOSITION EXPERIMENTS

The purpose of our deposition studies was to understand the effects that turbulent mixing has on deposition of PM_{10}. Glycerol ($C_3H_8O_3$) and distilled water H_2O were aerosolized using an UHS (Ultra Sonic Humidifier) (Model V5100NS, Kaz Inc., Hudson, NY). Various ratios of glycerol and distilled water were tested to produce particles with a mean volume diameter (MVD) between 0.54-9.0 μm (PM_{10}). The ratio that proved to fit closest to this range was a mixture of 20% glycerol to 80% distilled water. Ultrasonic nebulizers like the one used for our experiments are desirable because they are capable of producing a monodisperse aerosol in which the particle size, shape, and density can be controlled [42]. Ultrasonic nebulizers produce a MMD (mean mass diameter) range of 0-10 μm which was desired for our study: understanding deposition enhancement of PM_{10} to vegetative surfaces, as well as the respiration effects due to PM_{10} inhalation. Ultrasonic waves propagate energy to the surface of the liquid by a vibrating piezoelectric crystal. Particles are monodispersed when capillary waves are fractured at the surface and the surface tension releases the fluid particle [42].

The glycerol and distilled water mixture was particularly desirable for our experiments because glycerol is soluble in water, it has a similar density (glycerol = 1261 kg/m^3 to water = 1000 kg/m^3), and it has a similar surface tension (necessary to break the particle from the capillary wave). Larger ratios of 50% glycerol and 50% distilled water were tested, but did not have the surface tension necessary to free the particle from the liquid surface in the USH. Unlike distilled water, the glycerol molecule does not evaporate quickly when aerosolized. Concentration measurements were taken at multiple distances downstream of the turbulence grid to determine when the water had evaporated off. It was determined that by the first location downstream of the turbulence grid (x = 1.04 m), the distilled water had evaporated off and only the glycerol particle remained.

In order to quantify deposition of a liquid aerosol onto substrate surfaces during our deposition experiments, a fluorescence measurement technique was needed. This was a

result of the liquid aerosol particles impacting onto the substrate, spreading across the surface, and mixing with the other deposited particles. The total particle deposition could not be quantified by simply counting total particles deposited, so fluorescein was used to resolve this issue.

A powdery fluorescein sodium salt ($C_{20}H_{10}Na_2O_5$, Sigma-Aldrich, St. Louis, MO) was completely dissolved into the solution of 20% glycerol/80% water. When the fluorescein, glycerol, and water solution was aerosolized, the distilled water evaporated completely while being advected downstream. The resultant particles that deposited onto the substrate were comprised of glycerol and fluorescein. The glycerol particle primarily acted as a carrier molecule for the fluorescein to attach to for deposition. Deposition of the fluorescein powder onto the substrate surfaces could then be calculated using a Fluorimeter (1420 Victor3V, PerkinElmer Inc., Waltham MA).

A.1 Wind Tunnel Setup

Deposition experiments were conducted in the full-scale stratified wind tunnel of the EFL (Environmental Fluids Lab). The USH was injected into the converging section of the wind tunnel by drilling a 0.635 cm hole on the bottom of the convergent section and pressure fitting 0.635 cm PEX (cross-linked polyethylene) tubing into the hole. The PEX tubing extended from the nozzle of the USH beneath the wind tunnel to the centerline inside the wind tunnel. At the top of the tubing a 0.635 cm brass elbow was pressure fit to direct the aerosol in the streamwise flow direction and allow the aerosol to behave like a point source. Deposition experiments were conducted both with and without a turbulence grid to understand the effects turbulent motions have on deposition. The turbulence grid was designed to have the same dimensions as the wind tunnel test section (height = 61 cm and width = 122 cm) so it would pressure fit to all four sides of the wind tunnel. The grid was placed at the throat of the converging test section to insure that the incoming air flow would be very smooth and straight before it came into contact with the turbulence grid. The turbulence grid, shown in Fig. A.1, was designed with a grid mesh M of 8.66 cm and bar thickness d of 2.54 cm, so that a solidity of 50% was achieved. The grid was machined using 2.54 cm solid-square acrylic rods (Regional Supply, Salt Lake City, UT) and patterned together with Weld-On acrylic adhesive (IPS Corp., Compton, CA). The deposition frame was placed at two downstream locations from the throat of the converging section for both grid and no-grid deposition experiments. The frame was made using extruded aluminum T-channel, aluminum sheet metal flanges, and 24 gauge aluminum

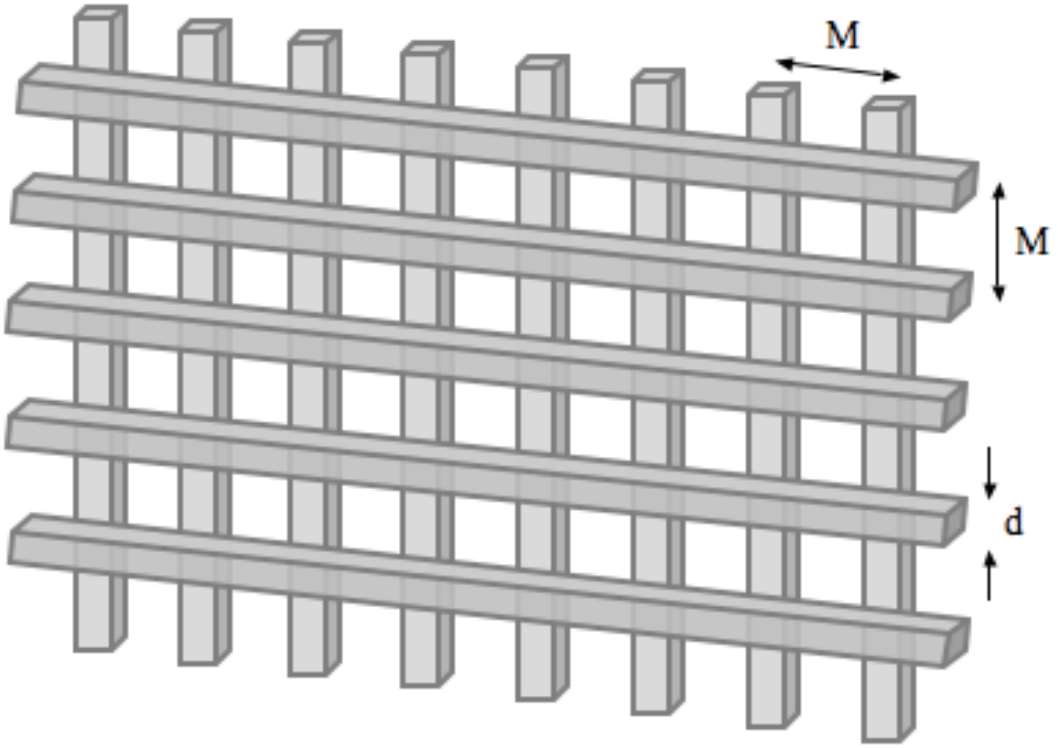

Figure A.1. The turbulence grid used for our wind tunnel studies on turbulent deposition was placed at the throat of the converging test section. M = 0.0866 m and d = 0.0254 m. (Not to scale).

wire. Fig. A.2 describes the deposition frame layout, as well as the substrate placement on the wire during the experiments. In order to facilitate a 6-axis deposition experiment and eliminate sheltering effects from each substrate, the substrate axes ($\pm x$, $\pm y$, and $\pm z$) were positioned approximately 1 cm from each other. This procedure was acceptable because the variation in aerosol concentration from one substrate location to the next was within the margin of the error bars. These deposition experiments were repeated three times for a specific downstream location, substrate size, and velocity to eliminate any inherent errors in aerosol concentration and allow for a more precise calculation of uncertainty. After each of the three experiments holding U, L_s, x constant, the substrate locations were rotated counterclockwise on the deposition frame and the experiment was repeated. This was performed three times since there were three axes (x, y, and z) to rotate the substrates across.The velocity measurements were varied by adjusting the pressure dial on the side of the wind tunnel, thereby changing the pitch of the turbine blade. A schematic of the wind tunnel layout for the deposition experiments is described in Fig. A.3.

A.2 Particle Concentration Measurements

The aerosol concentration measurements were taken at the same position (x ,y ,and z coordinate) as the deposition frame during the deposition experiments. Two locations downstream of the turbulence grid (x = 1.80 m and 2.13 m) were selected because a certain distance x/M $\approx$ 10 was needed for the turbulence to develop. Three velocities (U = 1.65, 4.84, 8.06 ms^{-1}) were chosen to simulate realistic velocities observed in the atmosphere. A Grimm 1.109 (mentioned previously) was used to record measurements at a flow rate of 1.2 L/min with an inlet of 0.32 cm. Isokinetic sampling calculations were performed for all three experimental velocities chosen using Eq. (A.1)

$$\frac{Q_s}{Q_o} = \left(\frac{D_s}{D_o}\right)^2. \tag{A.1}$$

Eq. (A.1) is a function of the sampling instrument flow rate Q_s, wind tunnel flow rate Q_o, sampling inlet area D_s, and wind tunnel frontal area D_o. At 1.65 ms^{-1} super-isokinetic sampling was calculated and sub-isokinetic sampling was calculated for both 4.84 ms^{-1} and 8.06 ms^{-1} velocity measurements. Change in over-sampling and/or under-sampling efficiency for particles 10 μm or less was shown to be smaller than 10% [37] from turbulent aerosol sampling. For our deposition results, little emphasis was placed on the isokinetic

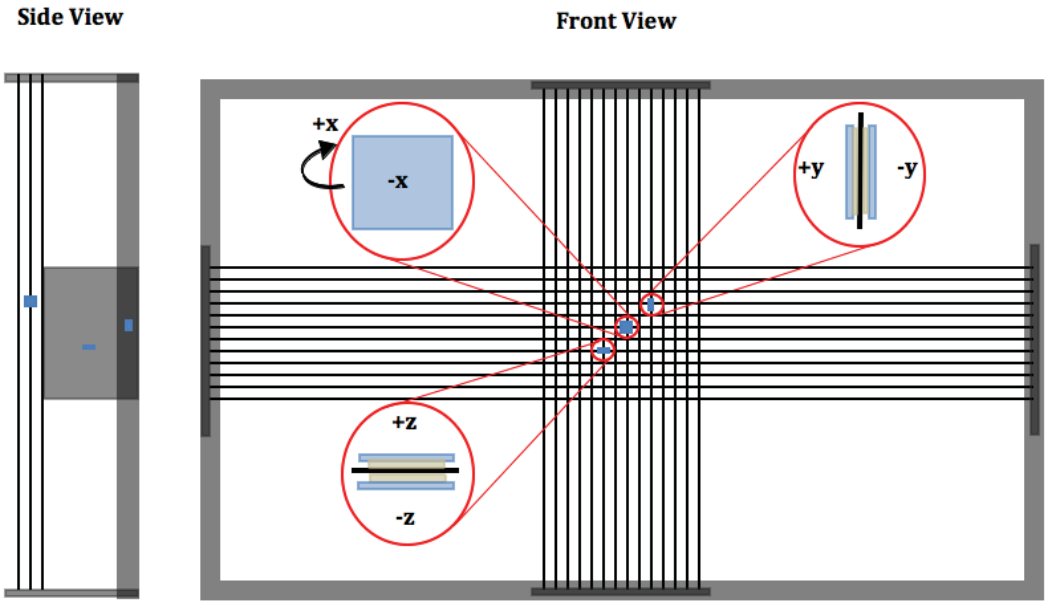

Figure A.2. Frontal and side view of the deposition frame used for our deposition experiments (Not to scale). After each of the experiments holding U, L_s, x constant, the substrates were rotated counterclockwise and the experiment was repeated.

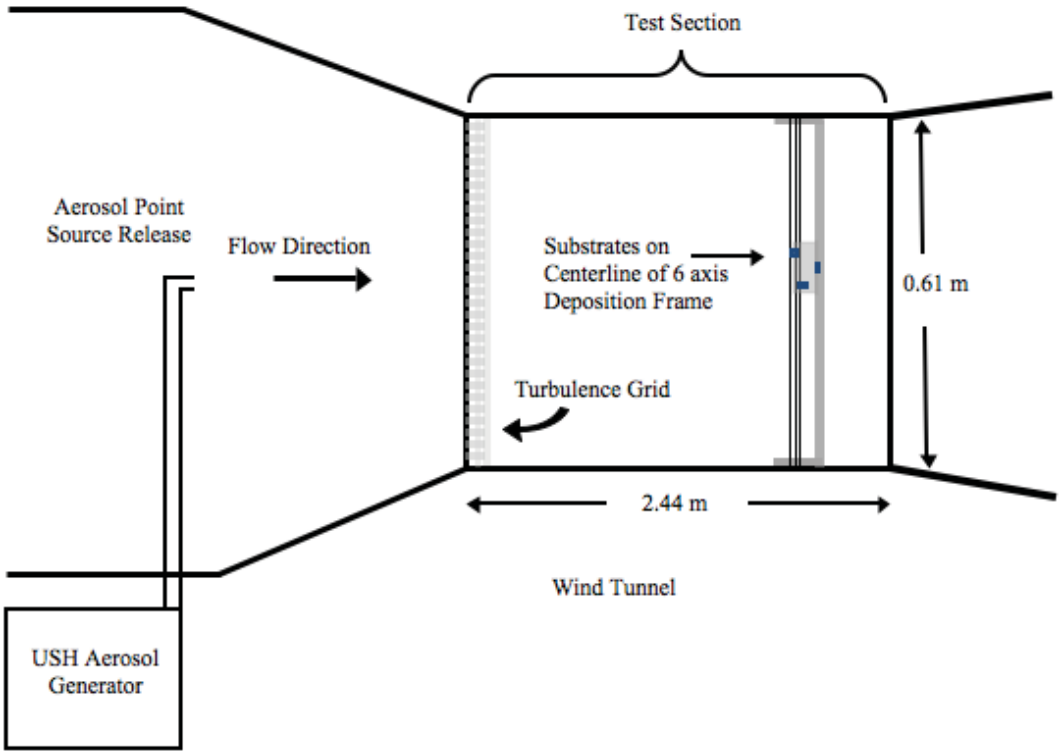

Figure A.3. Wind tunnel schematic showing placement of USH aerosol generator, turbulence grid, and deposition frame (Not to scale).

sampling of the Grimm 1.109 because our USH produced a mean particle diameter of 3.43 μm. Therefore minimal errors in turbulent sampling efficiency from sub-isokinetic and super-isokinetic sampling were not expected to bias our results. Also, the particle distributions from sub-isokinetic to super-isokinetic sampling were identical, indicating that all particle sizes were being accounted for.

The concentration measurements were averaged over 30 min periods at a 1 minute sampling rate in Count mode to acquire a good approximation of the concentrations during the deposition experiments. All concentration profiles had similar MVD distributions for all three velocity measurements and two locations from the turbulence grid. This is shown in Fig. A.4 for locations at 1.80 m and 2.13 m from the grid. The Grimm recorded data for 31 different bin sizes in units of counts/m^3 and was converted to a volumetric concentration (C_v) by multiplying counts/m^3 with the particle volume using the representative bin midpoint diameter (d_m). These volumetric concentrations are then multiplied by the mass concentration of the fluorescein used (2.5x10^6 mg/m^3) in the aerosol solution and summed over the known particle range (0.54 μm to 9.0 μm) of the aerosol to get a total mass concentration (ΣC_m) of fluorescein per volume of air (mg/m^3). C_m of the individual bins are normalized by ΣC_m to yield the PDF f($\overline{C}_m$) of the particle mass concentration. The mean particle diameter ($\overline{d}_p$) is then computed using Eq. (A.2)

$$\overline{d}_p = \sum_{m=0.54}^{9.0} (d_m \cdot f(\overline{C}_m)). \tag{A.2}$$

For both locations where deposition experiments were conducted $\overline{d}_p$ was found to be 3.43 μm and the standard deviation of the mean particle diameter was calculated $\sigma_d = \pm$ 1.53 μm using Eq. A.3.

$$\sigma_d = \left[\sum_{m=0.54}^{9.0} \left((d_m - \overline{d}_p)^2 \cdot f(\overline{C}_m) \right) \right]^{1/2}. \tag{A.3}$$

Note that all concentration measurements performed with the Grimm 1.109 did not actually incorporate fluorescein powder into the aerosol solution because fluorescein has an emission frequency of $\sim$515 nm that interferes with the laser-beam particle-counter and creates known errors in the particle count and distribution. The Grimm uses a light-scattering technology to estimate the signal coming from the particle as it passes through the laser-beam, so

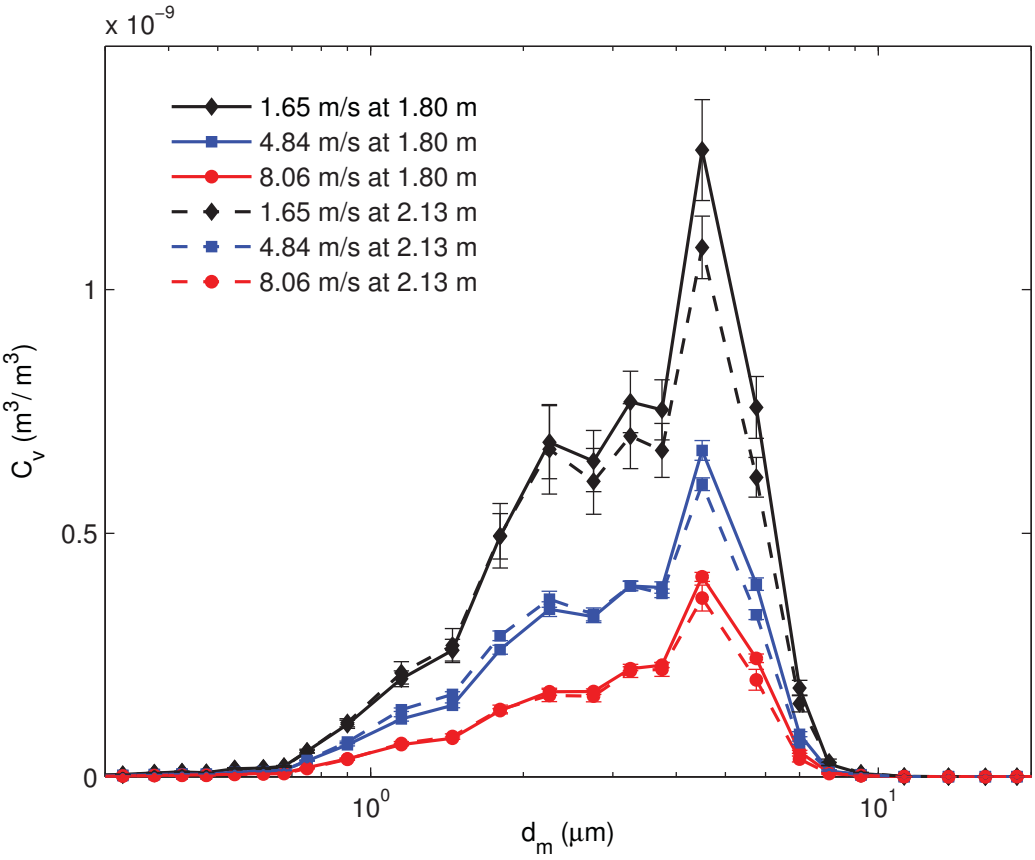

Figure A.4. Volumetric concentration for the glycerol/water aerosol produced by the USH at all three velocity measurements. Data were taken at distances $x = 1.80$ m (–) and $x = 2.13$ m (– –) from the turbulence grid.

additional fluorescence from a particle is a definite problem. The absence of fluorescein in the aerosol solution during concentration measurements did not affect the concentration distribution of the aerosol in any way because the concentration of fluorescein, relative to glycerol and water, was very low.

A.3 Dilution Series Calibration and Washing Procedure

Development of a calibration curve required a dilution series of concentrated fluorescein in distilled water to be performed before the deposition fraction of the fluorescein/glycerol particles could be quantified. For all dilution measurements a standard volume of 75 μL were pipetted into a 12 by 8, 100 μL well test plate to have consistent fluorescent levels from dilution to dilution. The series was diluted by (1/2) for each consecutive dilution starting with from a concentration of 0.5 mg of fluorescein per mL of distilled water and diluting down to 1x10^{-11} mg of fluorescein per mL of water. This dilution series required that 18 wells be filled on the test plate to achieve this range of 0.5 to 1x10^{-11} mg of fluorescein per mL of water. Once the dilution series was complete the 100 μL well test plate was placed in a Fluorimeter (1420 Victor3V, PerkinElmer Inc., Waltham MA) for fluorescent analysis. Using the fluorimetry software (Walac 1420 Workstation, PerkinElmer Inc., Waltham MA), the Fluorimeter output a fluorescent intensity (FL) level from each well. FL is a measure of the intensity of the fluorescent molecules after being excited by a certain spectrum of light. Results from the Fluorimeter showed that the dilution series covered the complete range of FL level from the lower limit of detection ($\sim$20,000) to the upper limit of saturation ($\sim$50,000,000). In between the upper and lower ranges of the dilution series a linear range existed where an empirical fit was developed in order to estimate the mass (C_w) of the fluorescein/glycerol particles in the washed solution. This is shown in Fig. A.5 where the red circles indicate the points that were used in the linear fit, given by Eq. A.4

$$FL = 1 \times 10^9 \cdot (C_w) - 94543. \tag{A.4}$$

The complete fluorimetry measurement technique (described earlier) required three general steps: 1) wash the substrates in distilled water 2) pipette the washed solution into 100 μL well test-plates and 3) measure the level of fluorescein intensity of the washed solution using a Fluorimeter. Following every deposition experiment, all six substrates were

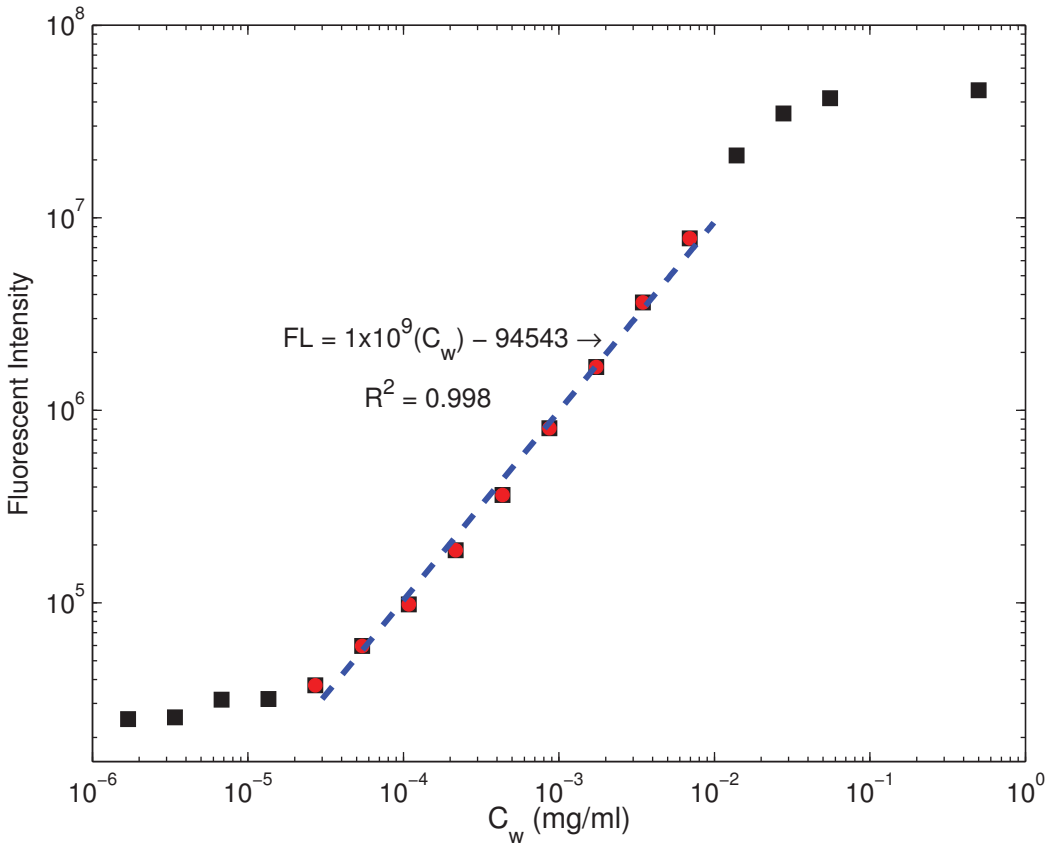

Figure A.5. Dilution series of fluorescent intensity versus the mass concentration of the fluorescein in solution. The equation from the linear range was used to quantify deposited fluorescein/glycerol particles.

immediately removed from the deposition frame and placed in separate test tubes. Each test tube (six per experiment) contained 2 mL of distilled water, used to wash away the fluorescein/glycerol particles from the substrate and suspend them in the water solution. Distilled water has a known FL level ($< 20{,}000$) that indicates how much fluorescent light is emitted when its electrons are excited by a light source (usually ultraviolet). Distilled water was chosen for its low fluorescence intensity levels and its ease of washing off the deposited fluorescein/glycerol particles from the substrates without interfering with the fluorescence level of the deposited particles. To limit any bias in the results that could have been caused by mishandling the fluorescein/glycerol laden substrates, small tabs (2 mm x 2 mm) were integrated on a corner of each substrate. Surgical clamps were then used to grab the substrate tabs off of the 24-gauge wire (on the deposition frame) and place into the test tubes. Before the substrates were set in the test tubes, the tabs were cut away so their contribution would not be accounted for in the deposition results. Individual test tubes were placed on a mini vortex mixer (Fisher Scientific, Waltham, MA) and pulsed for 20 seconds to ensure a uniform concentration of water, glycerol, and fluorescein was present before this solution was pipetted into a 100 μL well test-plate. To maintain accurate fluorescent intensity values to those measured in the dilution series, a volume of 75 μL of the washed solution was pipetted from each test tube. This pipetting procedure was done twice for each test tube to average out large errors associated with pipetting. (Note: For future washing procedures, pipetting should be performed at least three times to improve accuracy and eliminate any outliers). When all six test tube solutions were pipetted twice each (12 total wells filled), the well test-plate was placed in the Fluorimeter. Values of fluorescein intensity were recorded for each well. Since the amount of distilled water used in the washing procedure is known, the mass of fluorescein/glycerol and hence deposition fraction onto the substrate could be determine by evaluating for C_w in Eq. A.4. Finally, to determine the absolute measure of mass deposited M_w (mg), C_w (mg/mL) was multiplied by two in order to account for the 2 mL of distilled water that was used to wash away the particles from the substrates.

A.4 No-Grid Experiments

The no-grid deposition experiments required 30 minutes of run-time in the wind tunnel. This was significantly less than the grid turbulence experiments because the concentrations were significantly higher. Therefore the fluorescence level of the deposited particles on the substrate reached a level of detection much faster. Longer run-times resulted in level

of saturation for the -x impaction surface. Since our research was focused on isotropic turbulence, the no-grid experiments were only conducted at 1.80 m downstream from the entrance of the test to have a benchmark for comparison with the grid-turbulence cases. The deposition fraction DF results (x = 1.80 m, U = 4.84 ms^{-1}, and L_s = 1 cm) for the grid and no-grid experiments are shown in Fig. A.6. Deposition fraction (DF) is a function of the absolute mass deposited M_w, mean velocity U, time t, area of the substrate A, and mass concentration C_m of the aerosol in the wind tunnel. DF was previously computed in Chapter 2, Eq. 2.1.

A.5 Grid Turbulence Experiments

The grid-generated turbulence experiments required twice as much run-time due to the well-mixed behavior of the turbulence being generated. In 1 hour of run-time fluorescent intensity levels were adequate to calculate deposition on all axes. The results of these experiments were the primary investigation of this research. The goal was to vary Stk by changing the mean velocity (U), substrate size (L_s), and deposition distance from the turbulence grid (x). However, to average out any errors due to the 1 cm positioning difference (discussed in A1) from one axis to another (see Fig. A.2), three experiments were run holding U, L_s, and x constant. For every three of these experiments performed an average DF was calculated for each axis. Therefore, a total of 36 individual experiments were conducted for all six axes totaling 216 DF results. The average DF results on all axes are presented in Table A.1 where DF was calculated using Eq. 2.1. The results from Table A.1 and Table 2.1, as well as those plotted in Fig. 2.1, were essential in showing enhanced deposition from grid generated turbulence versus no grid turbulence, the deposition behavior on the nonimpaction surfaces ($+x$,$\pm y$,$\pm z$) with varying velocities, and the scaling effect of R_λ on the impaction surface ($-x$).

The deposition velocities v_d (cm s^{-1}) for all six axes were computed in Eq. A.5 to compare with similar deposition velocities measurements in other turbulence studies.

$$v_d = \frac{M_w}{C_m \cdot t \cdot A} \tag{A.5}$$

Here, the deposition velocity is defined as the ratio of deposited mass flux to the undisturbed mass concentration. The deposition velocity can be used to calculate DF as well by simply dividing v_d by the mean velocity U and multiplying by 100 to get a fraction of deposited

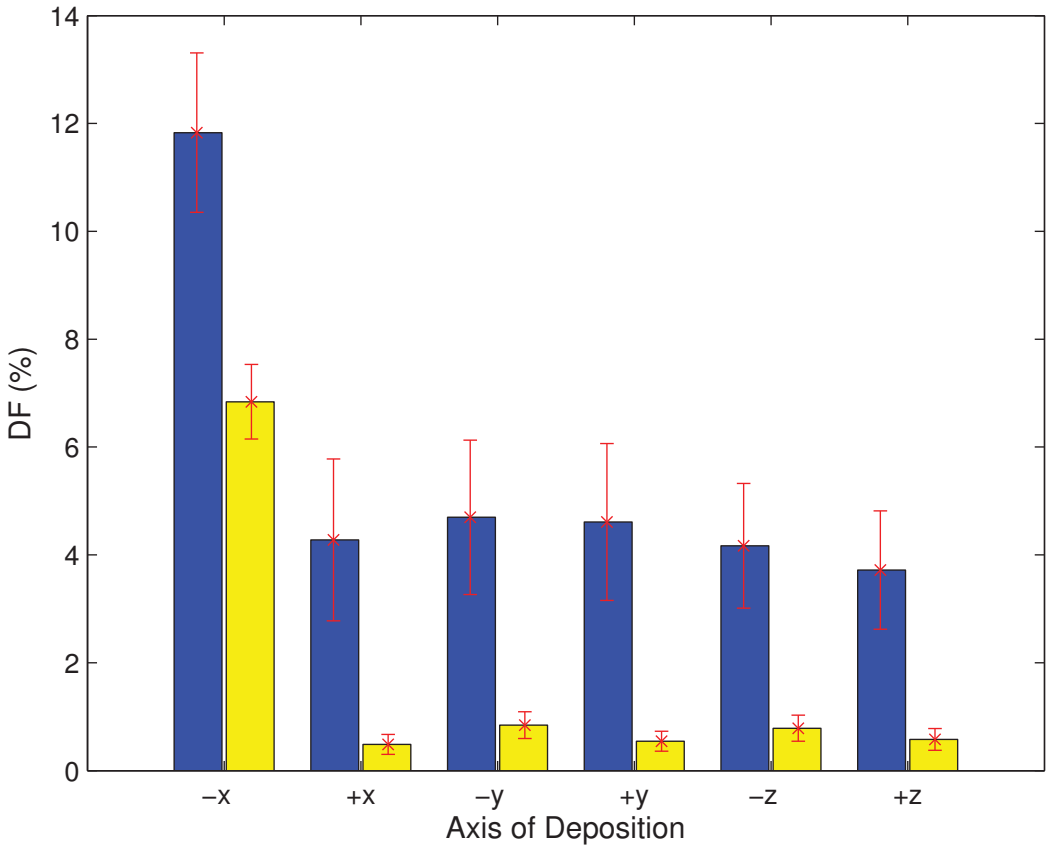

Figure A.6. Deposition results for the grid and no-grid experiments were taken at 1.8 m from the test section entrance, at 4.84 ms^{-1}, and using a substrate length of 1 cm.

Table A.1. $DF(\%)$ on all six substrate axes are shown for grid-generated turbulence at U = 1.65, 4.84, and 8.06 ms^{-1}. The substrate lengthscales (L_s) were 0.5, 1.0, and 1.4 cm and deposition results were all taken at x = 1.80 m and 2.13 m from the turbulence grid. The error bars refer to the uncertainty from the error propagation in calculating Stk and DF.

		Deposition Fraction (%) ± error at x = 1.80 m from grid					
U (ms^{-1})	L_s (cm)	$-x$	$+x$	$-y$	$+y$	$-z$	$+z$
1.7	0.5	13.6 ± 6.6	12.7 ± 6.7	12.6 ± 6.6	12.7 ± 6.6	13.1 ± 6.6	13.8 ± 6.8
4.8	0.5	44.3 ± 4.4	10.1 ± 5.2	12.7 ± 5.2	12.9 ± 5.4	22.8 ± 8.3	11.5 ± 4.9
8.1	0.5	97.4 ± 15.9	12.9 ± 6.3	13.5 ± 6.3	14.4 ± 6.5	15.0 ± 6.8	14.9 ± 6.6
1.7	1.0	5.7 ± 1.9	3.8 ± 1.7	4.1 ± 1.8	4.6 ± 1.7	4.3 ± 1.9	4.1 ± 1.7
4.8	1.0	11.8 ± 1.5	4.3 ± 1.5	4.7 ± 1.4	4.6 ± 1.5	4.2 ± 1.2	3.8 ± 1.1
8.1	1.0	31.2 ± 1.5	3.0 ± 1.3	4.0 ± 1.4	4.2 ± 1.2	4.4 ± 1.4	4.3 ± 1.3
1.7	1.4	2.7 ± 0.9	2.3 ± 1.0	2.3 ± 1.0	2.1 ± 1.0	2.4 ± 1.0	2.3 ± 1.0
4.8	1.4	4.0 ± 0.6	1.6 ± 0.7	1.9 ± 0.7	2.4 ± 0.7	2.2 ± 0.7	1.9 ± 0.5
8.1	1.4	9.8 ± 0.6	1.5 ± 0.7	2.1 ± 0.6	2.2 ± 0.7	2.5 ± 0.8	2.1 ± 0.7
		Deposition Fraction (%) ± error at x = 2.13 m from grid					
U (ms^{-1})	L_s (cm)	$-x$	$+x$	$-y$	$+y$	$-z$	$+z$
1.7	1.0	3.7 ± 1.8	3.3 ± 1.7	3.8 ± 1.6	3.8 ± 1.5	3.8 ± 1.7	3.7 ± 1.7
4.8	1.0	6.2 ± 1.2	2.7 ± 1.2	4.1 ± 1.6	4.6 ± 1.5	3.1 ± 1.1	3.8 ± 1.3
8.1	1.0	24.5 ± 1.9	3.4 ± 1.5	5.0 ± 1.6	4.8 ± 1.3	4.1 ± 1.3	4.5 ± 1.8

particles. Given that this is an important parameter in deposition measurements, our experimental results were compared with other studies on deposition velocities shown in Fig. A.7. Over the course of our experiments, we only tested one mean particle diameter size ($d_p = 3.43$ μm), so our results followed along a vertical line when deposition velocity is plotted versus particle diameter. Experiments from Sehmel (1980) and Moller and Shumann (1970) tested deposition of dry particles on a water surface in a wind tunnel. Results have shown that for a particle range of 2-20 μm deposition is generally governed by inertial impaction [27], which was the primary deposition mechanism for our experiments. In the larger size range (d_p>20 μm) deposition is primarily dominated by gravitational settling since the settling velocity increases with the square of the particle diameter [27]. This was most likely why our particles did not show any preference for DF in the $+z$ direction.

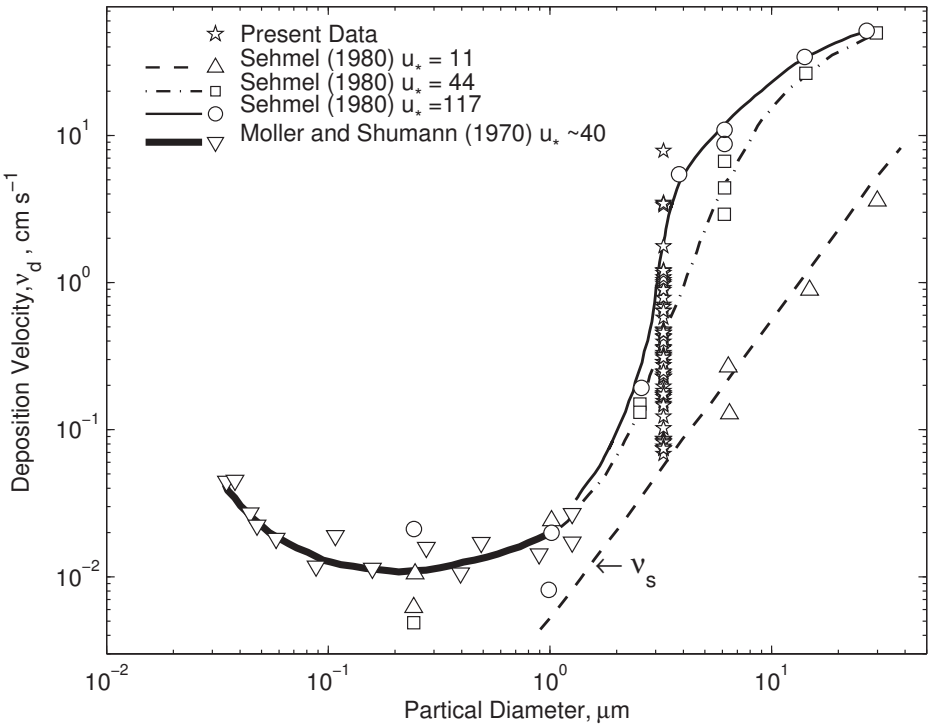

Figure A.7. Deposition velocities for our experiments with grid-generated turbulence. Measurements are collected using all three velocities in this study (U = 1.65, 4.84, and 8.05 ms^{-1}) with all three substrate sizes (L_s = 0.5, 1.0, 1.4 cm) (Slinn et at. 1978)

APPENDIX B

TURBULENCE EXPERIMENTS

A single sensor hotwire probe (55P16 Probe, Dantec Dynamic Inc., Denmark) was placed in the wind tunnel to gather turbulence data that correlate deposition enhancement to the proper scales of turbulence in the wind tunnel. Typically the Taylor microscale Reynolds number (R_λ) is used to characterize grid turbulence [29]. Therefore, hotwire probes were used to calculate R_λ by finding the r.m.s. of the instantaneous velocity (u) and the Taylor microscale (λ). At these smaller scales the eddy sizes of the microscale are expected to interact with the aerosol particles and contribute in actively depositing these particles to the substrate surfaces. These eddies are still capable of transferring energy to much smaller dissipative scales. Therefore, we believe λ should play an important role in characterizing deposition onto known surfaces.

Prior to turbulence data collection, the hotwire probe was calibrated using the University of Utah calibration test facility #2 before each experiment. Data were sampled at 25 kHz using an AN 1003 Anemometry system (AA. Lab Systmes Ltd, Israel), a BNC 2110 I/O ADC (National Instruments Inc., Austin TX), an NI PCI 6122 DAQ (National Instruments Inc., Austin, TX), NI Developer Suite software (Labview Version 10, National Instruments Inc., Austin TX), a model 2125 oscilloscope (BK Precision, Taiwan), and an HP Pavilion 64 bit desktop (Hewlett Packard, Palo Alto CA). A 10 torr pressure transducer (MKS Baratron Type 298 with MKS Baratron Type 270B Signal Conditioner, Andover MA) and hotwire probe were collocated at the exit of the converging calibration facility and a third order polynomial fit was applied in order to develop a calibration curve and equation for the wind tunnel measurements [32, 36]. Hotwire calibration was performed both before and after the data were acquired in the wind tunnel and the average of the two calibration equations was used in the final data analysis. Data were then taken at five separate locations in the test section of the wind tunnel, two of which were the exact locations of the deposition measurements.

B.1 Hotwire Calibration

The single sensor hot wire probe used for turbulence measurements was made of a 5 μm diameter tungsten wire which was soldered to the hotwire prongs and etched. The wire spacing between the hotwire prongs was 1.2 mm. To acquire data with the hotwire we used the electronic circuitry of the AN 1003 to maintain a constant probe temperature. This type of anemometry is known as CTA (Constant Temperature Anemometry). The other popular choice in anemometry systems is known as a CCA (Constant Current Anemometry) which keeps the current constant across the probe. Using the CTA system, the fluid (air) flows past the probe causing it to be cooled constantly. The probe has a Wheatstone bridge circuitry setup so that as the fluid cools the probe a change in resistance on the resistor arm can be measured. The anemometer maintains the temperature of the probe by adjusting for the rate at which the probe is being cooled (i.e., velocity of the fluid) and measuring the voltage difference caused by the change in resistance on the Wheatstone bridge. This corresponding voltage difference caused by the velocity of the fluid over the probe goes through signal conditioning to reduce the noise in the voltage signal. The voltage output has a nonlinear relationship with the fluid velocity. Therefore a pitot tube is used to calibrate the measured velocities from the pressure transducer against the measured voltages from the hotwire. In the CTA mode, the hotwire operated at an overheat ratio of 1.5. The signals were sampled at $f_s = 25$ kHz, lowpass filtered at a frequency of 10.4 kHz and digitized with a 16 bit analog to digital converter. The sampling time was 60 second, so the total number of data points per measurement at every location and speed was 1.5 x 10^6.

Rather than using a more accurate *in situ* method to calibrate the hotwire in the wind tunnel where the turbulence data was recorded, the portable jet calibration facility #2 was used to calibrate the hotwire probe. After calibration the probe was then placed in the wind tunnel for data collection. The time and simplicity in using the calibration facility were the primary reasons for this choice. On the calibration unit, there were two fan settings (low and high) available. The high fan setting (Comair Rotron Patriot) was used for the calibration because it could reach higher velocities $\sim$10 ms^{-1} that were required in the wind tunnel, whereas the low fan (Comair Rotron Whisper) setting could only reach speeds up to $\sim$2 ms^{-1}. The fan speed was varied by adjusting the voltage of a HP programmable power supply (Hewlett Packard, HP6632A, Palo Alto CA). As flow entered the calibration unit at the end of the fan, it passed through a diffuser, a settling chamber, four flow straightening sections, honeycomb, fine screen, coarse screen, and exited at a contraction with a rectangular orifice. This ensured that the flow coming in contact with the hotwire

probe, pitot tube, and thermocouple would be completely laminar. The calibration flow speeds were measured using a pitot static tube attached by plastic tubing to a differential pressure transducer that outputs a voltage where 1 Volt = 1 mmHg. Bernoulli's equation was programmed into Labview to calculate the velocity. Ambient air temperature was calculated simultaneously using a type T thermocouple to account for the temperature variation from the beginning of 1st calibration to the end of the 2nd calibration. This change in temperature (ΔT) was accounted for in order to correct the turbulence measurements from the hotwire inside the wind tunnel.

The hotwire probe was connected by a hotwire support rod at the orifice exit of the calibration facility #2. The pitot static tube was collocated to a support rod next to the hotwire and at attached, by plastic tubing, to a differential pressure transducer. The thermocouple was mounted on the orifice exit edge to get an estimate for the temperature coming out of the calibration unit. The hotwire probe had a BNC (Bayonet Neill Concelman) connector that went to an input in the AN 1003 Anemometry system and a BNC connector output that signal from the AN 1003 to the input (ai0) of the NI 2110 ADC (Analog to Digital Converter). The pitot tube was attached to an inlet on the pressure transducer and the pressure transducer had a BNC output (analog signal from signal conditioner) that connected to the input (ai1) of the NI 2110 ADC. The thermocouple had a BNC connector that attached directly to the analog input (ai2) of the NI 2110 ADC. Once all BNC connectors were attached to the NI 2110, a cable connected to the NI 6122 DAQ (Data Acquisition Unit) which communicated with the NI Developer Suite software. This software used Labview 10 to process the incoming digital signals from the hotwire, pitot tube, and thermocouple and output the data as text files to the computer. Matlab 7.10 was then used to process the data from the text files.

For calibrating the hotwire probe with the pressure transducer the steps were as follows:

1. Checked that BNC connections, hotwire probe, pitot tube, thermocouple, circuitry, and plugs were connected appropriately as described in the above two paragraphs.

2. Turned on the AN 1003 and followed the green manual entitled "Automated Hotwire Calibration User's Manual." This was located on top of the AN 1003 system and gave a detailed description of how to calibrate the channel of the CTA (i.e., set OHR (Over Heat Ratio), sampling frequency, DC offset, and Gain). Once all 28 steps were complete, the hotwire was ready for calibration with the pitot tube.

3. Let the AN 1003 system warm up for 5 hours because there was a voltage drift at the channel output caused by the warming up of the electronics. After 5 hours the calibration was started.

4. Turned on the HP Pavilion and opened the file on the desktop titled $Nate_S ean_D AQ$. Then clicked on the *Calibration* file to load Labview 10. This was the script written specifically for this calibration.

5. Opened the Labview *Calibration* file and input the temperature and pressure into the Front Panel using the wall thermometer/barometer located next to the wind tunnel. The number of samples was set to 1,500,000 because the sampling frequency was set to 25 kHz and 1 minute of turbulence data was desired. (Note: convergence occurred after 30 seconds of data collection).

6. Turned on HP power supply and set current and voltage using *iset* and *vset*, respectively. To ensure the range of velocities chosen in the wind tunnel (1.65-8.06 ms^{-1}) could be calculated, 11 different voltages from the power supply were selected (5-20 Volts) to vary the fan speed of the calibration unit between $\sim$1.2 ms^{-1} and $\sim$8.7 ms^{-1}.

7. Ran the *Calibration* file for every voltage increment and recorded average voltages from the hotwire and average velocities from the pitot tube.

Once steps 1-7 were completed the 11 raw calibration data from the hotwire and pitot tube measurements were fit to a power law equation using King's Law:

$$\mathrm{E}^2 = \mathrm{A} + \mathrm{BU}^n. \tag{B.1}$$

Using Matlab's nonlinear, least squares solver (*lsqcurvefit*) a Levenberg-Marquardt method was used to numerically solve for the unknown parameters A, B, and n in Eq. B.1. Calibration measurements were taken both before and after turbulence data were acquired in the wind tunnel. This was performed in order to account for the voltage drift that occurred over the course of the data collection. The voltage drift was most likely caused by the increase in temperature over the two-hour period of data collection in the wind tunnel (between initial calibration and final calibration). The temperature increased by 2 °C from initial (24 °C) to final (26 °C) calibration. Since temperature measurements were only taken during the initial and final calibrations and not during the data collection in the

wind tunnel, an exact temperature correction was not possible. Instead, a simple average of the two calibration curves was used to fit with our turbulence data. The average fit was chosen because turbulence data for x = 1.80 m and x = 2.13 m were collected about half way (∼1 hr) into the two-hour experiment. Since these distances were also locations where the deposition experiments were performed, it seems reasonable to assume that the average curve fit would give the most accurate calculations of the turbulence data and corresponding deposition calculations. This justification assumes a linear increase in temperature from initial to final calibration. The raw data for the initial, final, and average calibrations are shown in Fig. B.1. Fig. B.2 shows the average curve fit to the raw data using King's Law (Eq. B.1). This average fit was used to solve for the velocity components of the turbulence data using Eq. B.2:

$$\mathrm{U} = \left(\frac{\mathrm{E}^2 \text{ - } \mathrm{A}}{\mathrm{B}}\right)^{1/n}. \tag{B.2}$$

So as not to be confused with the mean velocity U, the U component calculated here is actually the instantaneous velocity, further denoted as u.

B.2 Hotwire Measurements and Turbulence Results

The instantaneous velocity component u can be decomposed into two parts, the mean component U and the fluctuating component u′ shown in Eq. B.3:

$$\mathrm{u} = \mathrm{U} + \mathrm{u}'. \tag{B.3}$$

These values (U and u′) are calculated within the Matlab script after data collection, where u′ is the r.m.s. (root mean square) of the instantaneous velocity u. The instantaneous turbulence data were collected at five different locations in the wind tunnel after initial calibration. To ensure that turbulence measurements could be correlated with the deposition results, these data were measured at the same x distance from the grid and at the same vertical height (approximately centerline). The first hotwire measurement was placed at the closest x location to the turbulence grid (x = 1.03 m) and velocities were increased from 1.65 ms^{-1}, to 4.84 ms^{-1}, and finally to 8.06 ms^{-1}. Labview recorded hotwire data for 1 minute at each velocity setting and between each hotwire measurement there was a 30

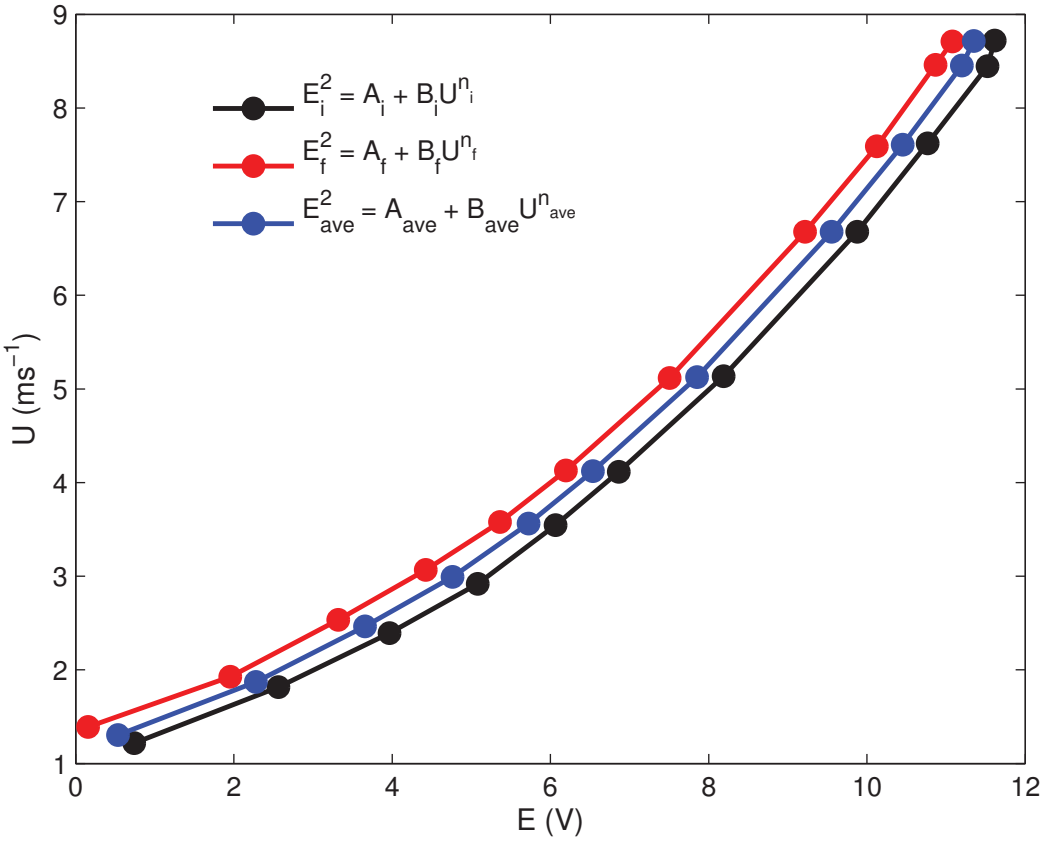

Figure B.1. Calibration of the hotwire probe with the pitot tube. Calibrations were collected both before and after turbulence quantification in the wind tunnel. The average calibration was determined to be the best curve to fit to our data.

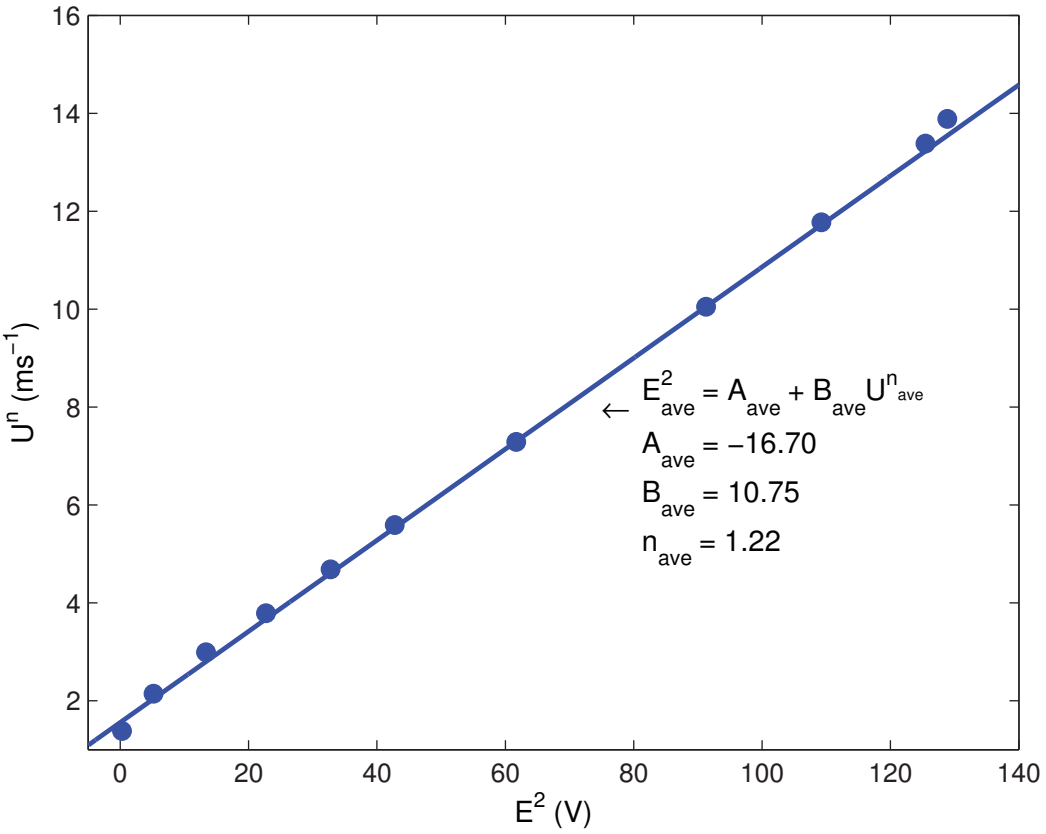

Figure B.2. The average calibration was used to acquire turbulence measurements from King's Law. Values of A, B, and n were not typical due to the voltage range (±10 V), DC offset (3.72 V), and gain (∼14.8) selected by the AN 1003.

second lag time in data collection. This to limit the error in velocity measurements from ramping up to the next velocity measurement. Fig. B.3 shows the 1 minute instantaneous time series measurements at U = 1.65, 4.84, and 8.06 ms^{-1} for the x = 1.03 m. Once data were collected at 1.65 ms^{-1}, 4.84 ms^{-1}, and 8.06 ms^{-1} for that x location the hotwire was placed at the next closest downstream location chosen. Five total downstream locations from the turbulence grid were measured (x = 1.03, 1.38, 1.80, 2.13, and 2.43 m) in order to completely describe the turbulence throughout the entire test section. The x/M value was an important variable in choosing the first location to take hotwire data. At x/M = 10 grid turbulence is said to be isotropic, but before that point the turbulence is still forming in the wake of the grid [31].

The x/M value where the first turbulence measurements were recorded was 11.9, therefore isotropic turbulence was expected. To check the isotropy of the turbulence a PDF (Probability Density Function) of the hotwire data was calculated [31]. A Gaussian (normal) distribution from the computed PDF would indicate that the turbulence is isotropic [32]. Gaussian statistics were calculated from the third and fourth order moments (i.e., skewness of 0.00 and kurtosis of 3.00, respectively). For the first x location (x/M = 11.9) a skewness of 0.08 and kurtosis of 2.96 were calculated (see Chapter 3 of Pope [31] for PDF statistics). This suggested that the turbulence created from the grid was isotropic by x/M $\sim$ 10. The PDF at the first x distance location for U = 5 ms^{-1} is plotted in Fig. B.4. After the hotwire data for all locations were processed, an interesting phenomenon of our grid was observed. Tennekes and Lumley [32] have shown that isotropy improves further down from a turbulence grid. However, the isotropic nature (i.e., PDF statistics) from our grid behaved quite the opposite. The skewness and kurtosis were calculated for all velocities from x = 1.03 m to x = 2.43 m, and it was evident that the turbulence diverged from isotropy farther down from the grid. Fig. B.5 has a skewness of -0.23 and kurtosis of 4.75 at x = 2.13 m and U = 4.84 ms^{-1}. Examination of the instantaneous time series velocity data for x locations at 1.80, 2.13, and 2.43 m showed much larger spikes or fluctuations occurring on the lower end of the time series velocity measurements for 4.84 ms^{-1} and 8.06 ms^{-1}. This is shown in Fig. B.6 at x = 2.13 m. Although it was not tested, the accepted hypothesis for this unexpected behavior was that a boundary layer formed on all four sides of the turbulence grid which caused the lower velocity fluid of the growing boundary layer to diffuse up into the hotwire probe. We believe that the flow was "tripped" or perturbed (forming the boundary layer) from four 1 cm thick plywood strips that were pressure fit against the walls of the entrance region in the wind tunnel. This was necessary because the turbulence grid

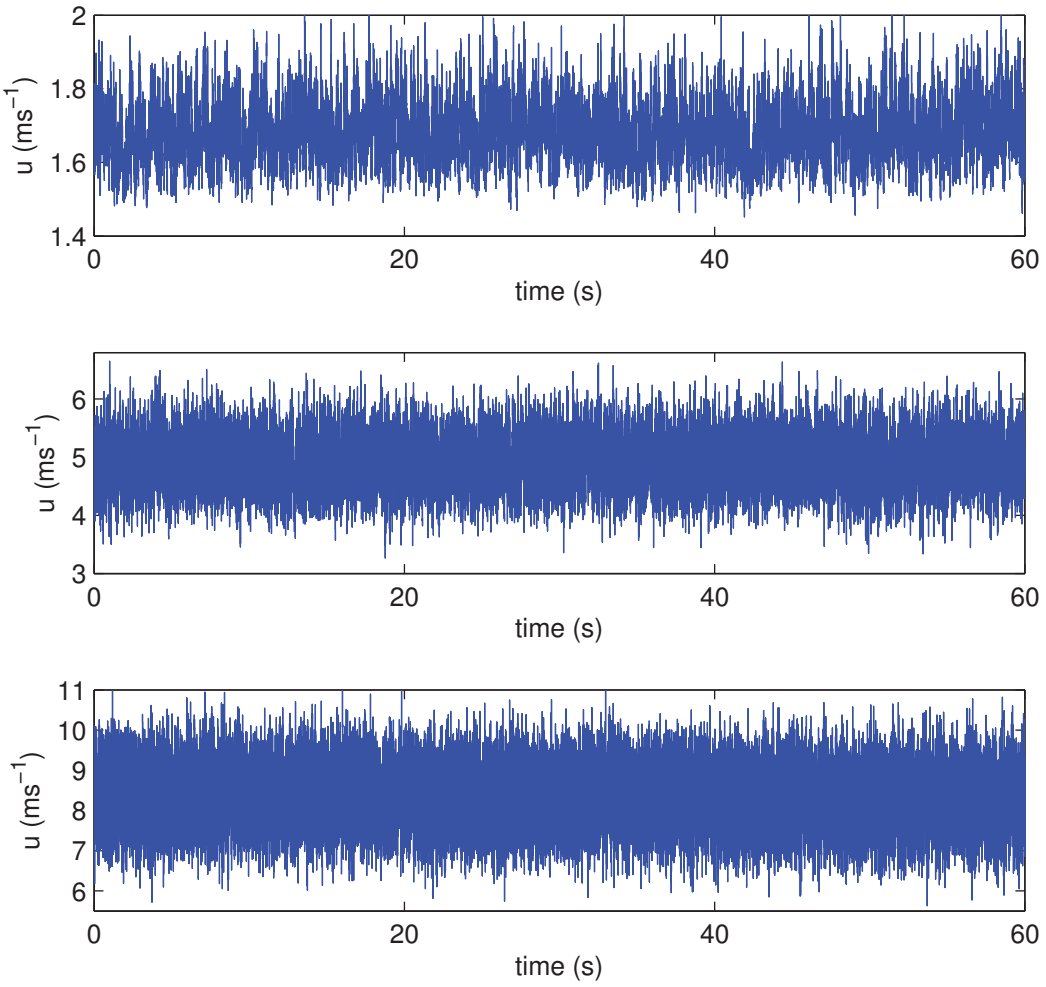

Figure B.3. Time series data of the instantaneous velocity u at U = 1.65, 4.84, and 8.06 ms^{-1} and 1.03 m from the turbulence grid.

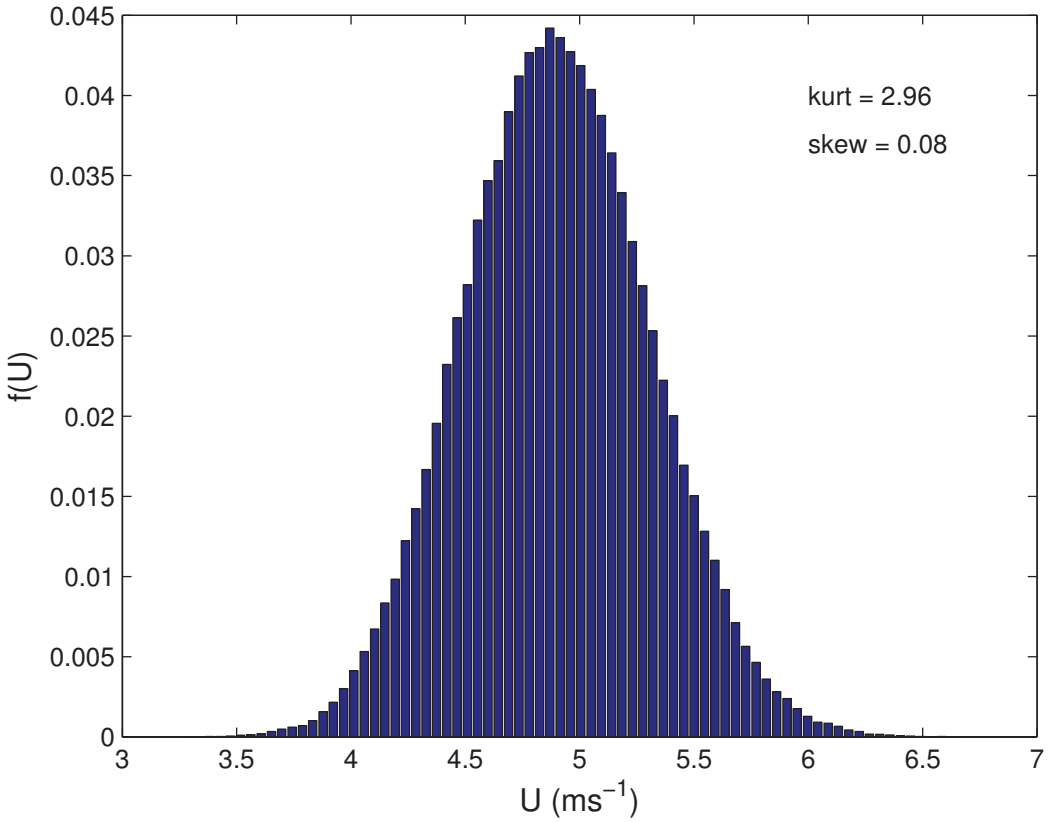

Figure B.4. Gaussian distribution for turbulence measurements acquired at U = 4.84 ms^{-1} and 1.03 m from the turbulence grid. This distribution indicates the presence of isotropic turbulence.

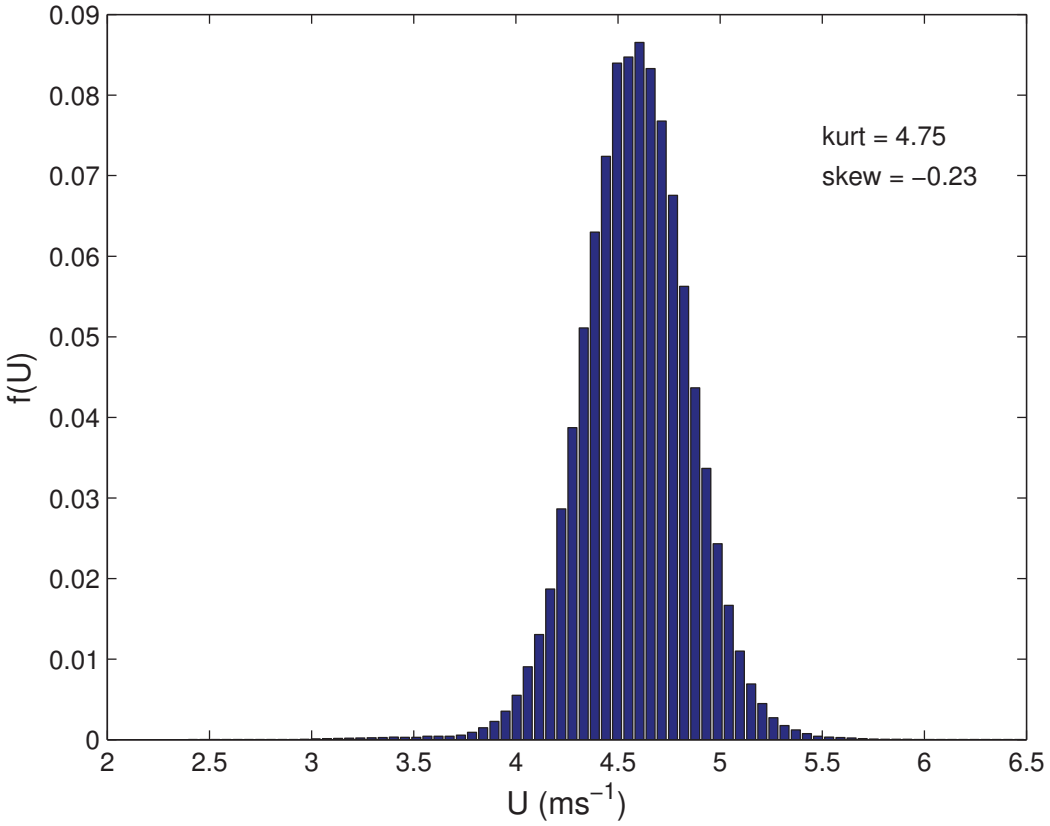

Figure B.5. Nongaussian distribution for turbulence measurements acquired at U = 4.84 ms^{-1} and 2.13 m from the turbulence grid. This distribution indicates that there was a departure from isotropy.

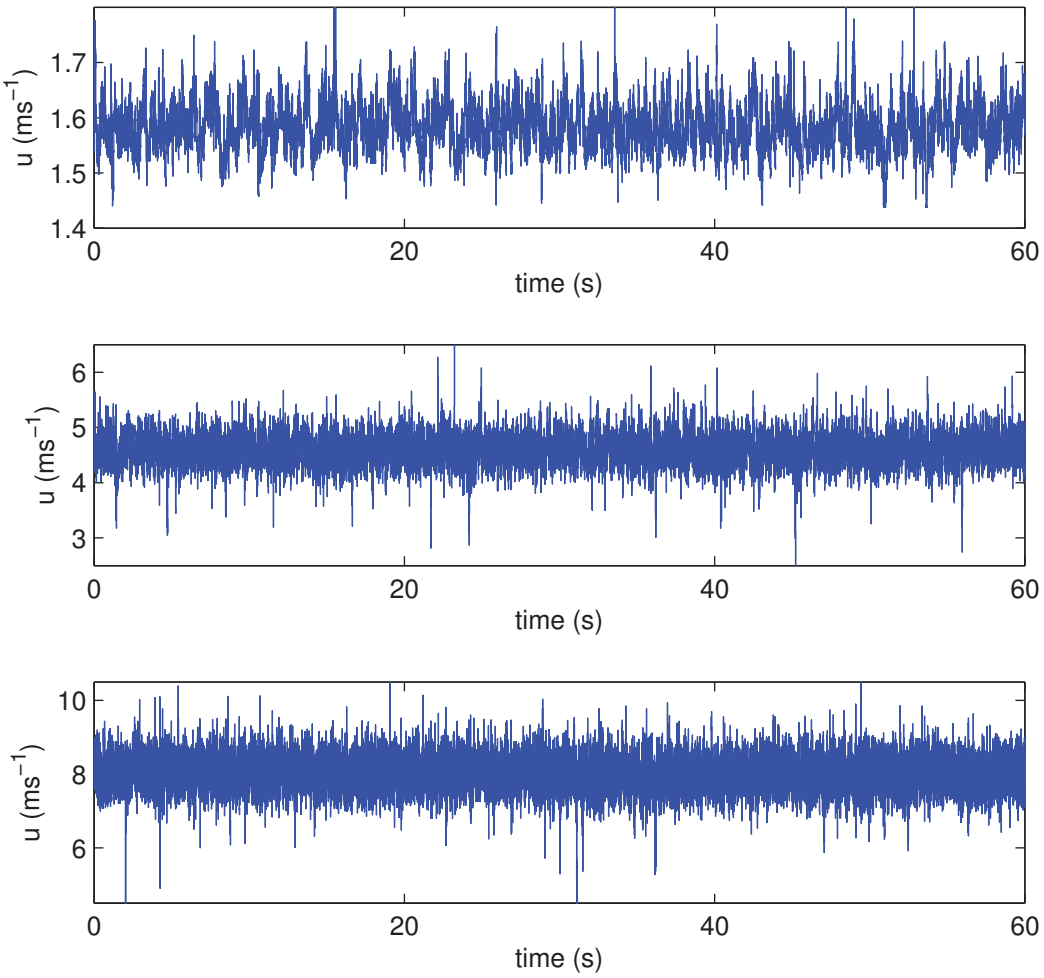

Figure B.6. Time series data of the instantaneous velocity u at U = 1.65, 4.84, and 8.06 ms^{-1} and 2.13 m from the turbulence grid. Large turbulent fluctuations were most prevalent on the lower ends of U = 4.84 and 8.06 ms^{-1}.

was too brittle to be pressure fit against the walls, so plywood was used to wedge the grid into place. For x = 1.80. 2.13, and 2.43 m the skewness for both 4.84 ms^{-1} and 8.06 ms^{-1} was always negative. However for U = 1.65 ms^{-1} the skewness was always positive at these x locations. Regardless, for all three velocities tested the turbulence diverged from isotropy at x = 1.80, 2.13, and 2.43 m. The plywood on the top and bottom of the wind tunnel have since been removed in hopes of improving the isotropy for future deposition and turbulence studies. Additional hotwire measurements are advised since the boundary layer should not affect future results.

The average velocity measurements (U = 1.65, 4.84, and 8.06 ms^{-1}), which have been used throughout the entirety of this paper, were calculated based on the average of the mean U at all locations. The mean U measurements in Fig. B.7 were statistically significant at every location because all values were within the range of the error bars.

The decay of isotropic *tke* (turbulence kinetic energy) or Reynolds stresses ($u_i u_i$) is an important feature of grid generated turbulence because it shows how energy is dissipated by the smaller eddies (Kolmogorov, η) in the flow. Grid generated flows have shown that ${u_1}^2$, ${u_2}^2$, and ${u_3}^2$ become independent of position in the spanwise direction of the flow and decay at x $\sim$10M from the grid. All three components of the flow have the same value at this distance and decay at the same rate until the final period of decay occurs and the isotropic turbulence becomes anisotropic. At the final period of decay where turbulence becomes anisotropic the larger (inertial driven) eddies of order M are dissipated out leaving behind the smaller (viscous driven) eddies on the order of η. As a sample of measurements, Fig. B.8 shows the variation in turbulence decay using similar grid meshes. The red $\circ$ are from the experiments of Comte-Bellot and Corrsin [30] where square 2.54 cm rods were used with a solidity of $\sigma = 44\%$ to produce a slope of $(x/M)^{-1.3}$. Owing to a larger grid solidity of $\sigma = 50\%$ that was used for our experiments (blue $\star$, $\diamond$, and $\times$), a slope of $(x/M)^{-1.1}$ was observed in Fig. B.8. For all three velocities in Comte-Bellot and Corrsin [30] (similar to our measured velocities) the decay of Reynolds stresses scaled the same in the initial period of decay, as the theory suggests [31]. However, the velocities from our experiments did not scale exactly the same, but were very similar at U $\geq$1.65 ms^{-1}.

B.3 Taylor Microscale Analysis

The Taylor microscale Reynolds number (R_λ) was chosen to scale with our deposition results because it is the typical Reynolds number used to describe grid generated turbulence [29]. Also, for any deposition in the presence of turbulence (i.e., deposition in the

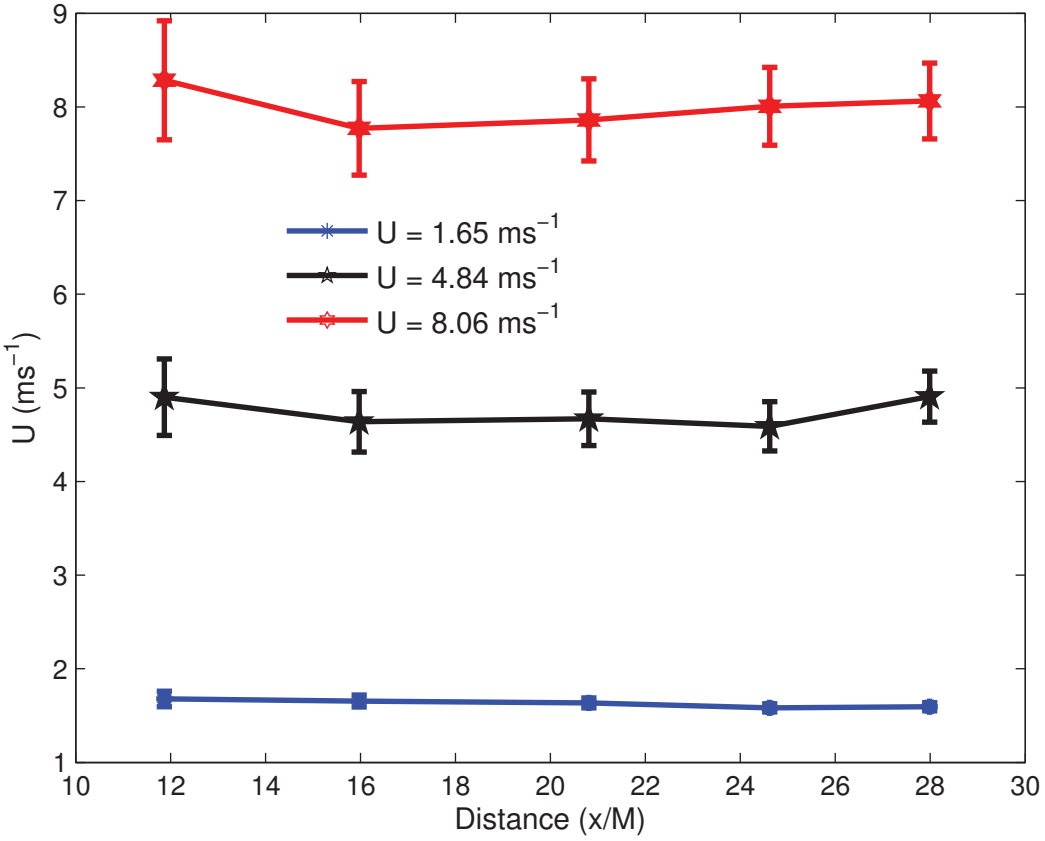

Figure B.7. Mean velocities U measured at five different locations from the grid. Error bars were calculated from the standard deviations of U.

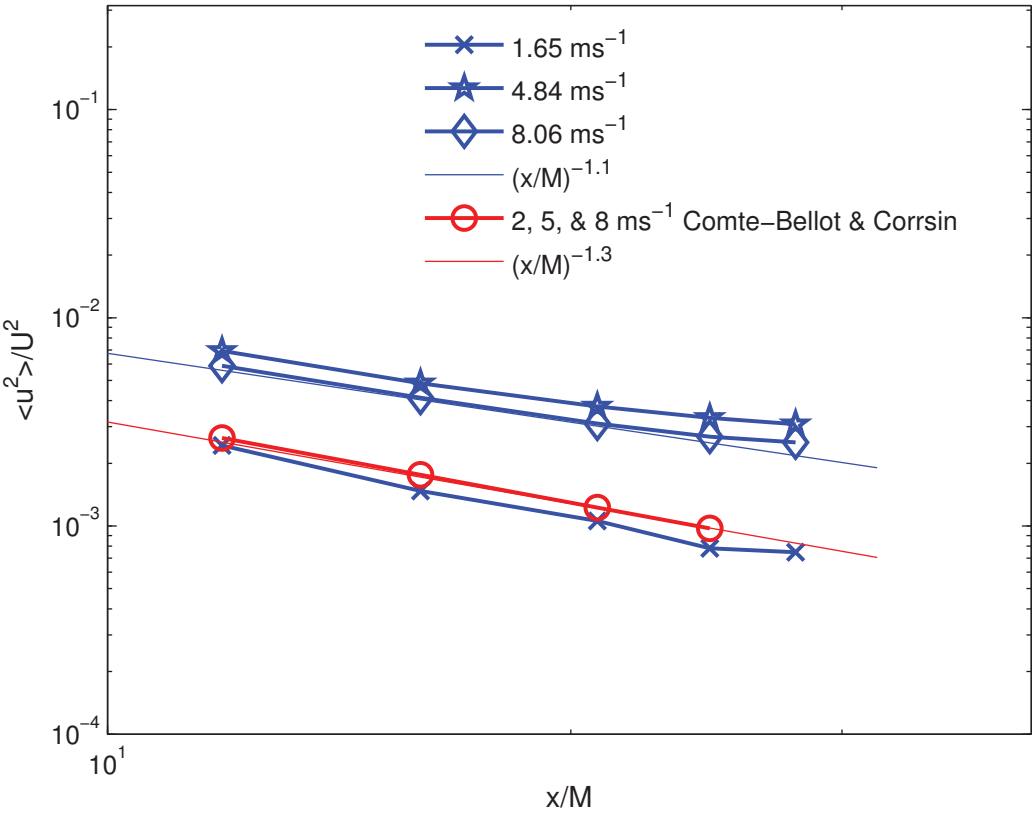

Figure B.8. Variation in the decay of *tke* using two similar grid solidities. Comte-Bellot and Corrsin had a grid solidity (σ) of 44% and our experiments used a solidity (σ) of 50%. Slightly different decay rates were observed as a result.

atmosphere), Stk fails to account for the turbulent fluctuations (u') or the smallest energy containing eddies (λ) that potentially transport the particles. These turbulence parameters are important because the fluctuations (u') act to transfer momentum to the smaller fluid particles [22] and the lengthscale λ is directly related to the average length of the increasing and/or decreasing u'. In section B.3 u' was found by calculating the r.m.s. of the streamwise velocity (standard deviation, σ_u). However, calculations of λ have yet to be described.

The Taylor microscale λ is found by fitting a parabola to the first few points at the origin of the autocorrelation function. For our turbulence data a parabolic polynomial regression to the first three points at the origin of the autocorrelation function ($\rho(s)$) [32, 31] were used to find λ, where $\rho(s)$ is given by Eq. (B.4):

$$\rho(s) = \langle \mathrm{u}'(t)\mathrm{u}'(t+s)\rangle / \langle \mathrm{u}'(t)^2\rangle. \tag{B.4}$$

In Eq. (B.4), $\mathrm{u}'(t)$ is the fluctuating velocity component at time t and $\mathrm{u}'(t+s)$ is the fluctuating velocity component at a time lag of t+s. Fig. B.9 is presented to give a better understanding of how well the parabola fit to the first three points of the autocorrelation function. A 2nd order polynomial regression was used to fit the parabola to the first three data points of the autocorrelation function. This was determined by the polynomial method of [A]{x}={b} described in Eq. B.5:

$$\begin{bmatrix} n & \Sigma x_i & \Sigma x_i^2 \\ \Sigma x_i & \Sigma x_i^2 & \Sigma x_i^3 \\ \Sigma x_i^2 & \Sigma x_i^3 & \Sigma x_i^4 \end{bmatrix} \begin{Bmatrix} a_o \\ a_1 \\ a_2 \end{Bmatrix} = \begin{Bmatrix} \Sigma y_i \\ \Sigma y_i x_i \\ \Sigma y_i x_i^2 \end{Bmatrix}. \tag{B.5}$$

The a_i terms were the coefficients of the fitted parabola, x_i were the chosen number of x points (in our case, 3 pts) in ρ fit to the parabola, and y_i were the chosen number of y points (in our case, 3 pts) in ρ fit to the parabola. Since a_o was forced to be 1 in order to fit the parabola to the origin of the autocorrelation, Eq. B.5 reduced to:

$$\begin{bmatrix} \Sigma x_i^2 & \Sigma x_i^3 \\ \Sigma x_i^3 & \Sigma x_i^4 \end{bmatrix} \begin{Bmatrix} a_1 \\ a_2 \end{Bmatrix} = \begin{Bmatrix} \Sigma y_i x_i - \Sigma x_i \\ \Sigma y_i x_i - \Sigma x_i^2 \end{Bmatrix}. \tag{B.6}$$

Finally, when the coefficients were calculated in Eq. B.5, a parabola was fit to the autocorrelation function using Eq. B.7:

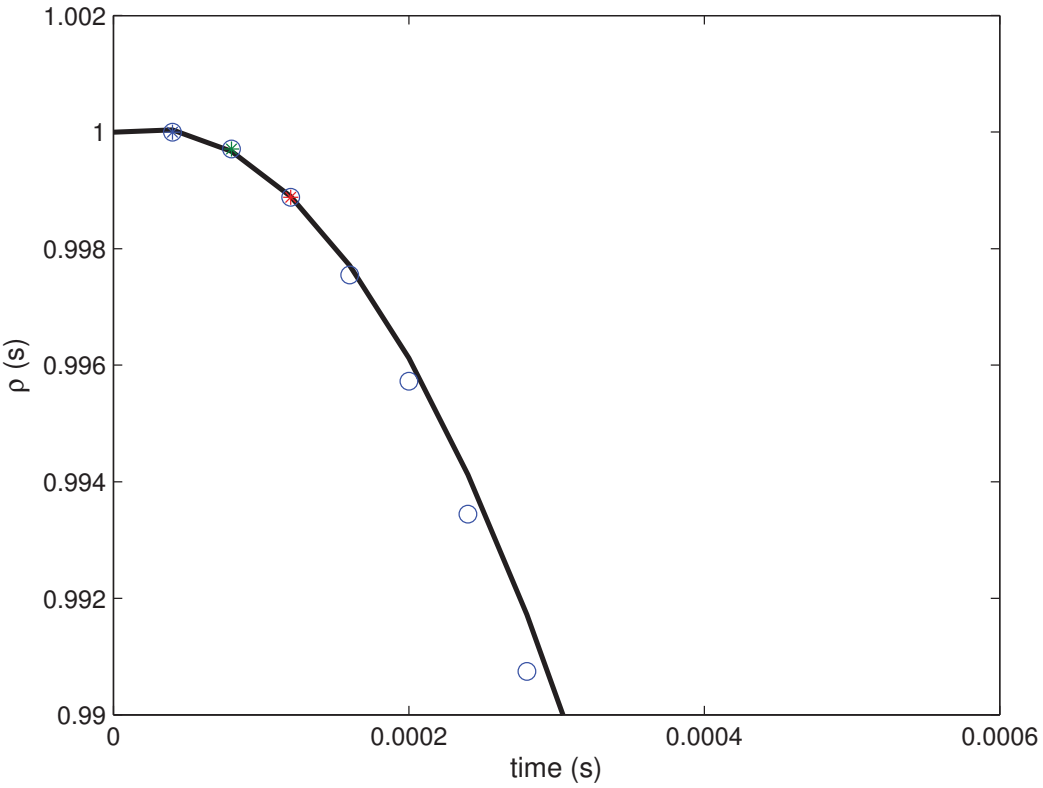

Figure B.9. The parabola was fit to the first three points of the autocorrelation function using a polynomial regression. This is a close up image of Fig. B.10.

$$y = a_o + a_1 x + a_2 x^2. \tag{B.7}$$

The location where the parabola crossed the x axis of the autocorrelation function was found to be the Taylor-microscale timescale λ_t, since this function was calculated in time and not space. The autocorrelation function and fitted parabola for U = 4.84 ms^{-1} and x = 2.13 m are shown in Fig. B.10. The Taylor-microscale timescale λ_t was found to be 0.0028 seconds. The lengthscale for the Taylor-microscale λ was then determined based on Taylor's frozen hypothesis which assumes that turbulence is "frozen" for continuous turbulence data measured from a single point. The idea behind this hypothesis is that as the mean flow advects past the hotwire probe in the wind tunnel, the fundamental properties of the eddies (i.e., λ) are unchanged or "frozen" in time and space. With that in mind, the lengthscale λ was calculated from Eq. B.8:

$$\lambda = \lambda_t \cdot U. \tag{B.8}$$

The size of the eddies λ grew over the length of the wind tunnel, from the x = 1.03 m to 2.43 m.

B.3.1 Scaling

The reasoning for scaling our deposition results by R_λ^n was to compare with the results from exact numerical solutions given by Marple and Liu [1] for deposition by impaction onto a flat plate. Thinking from a very fundamental perspective, the argument in favor of scaling our results by a turbulence parameter was that both experiments used the same flat plate impaction setup. However, they had two different flow regimes (laminar and turbulent) responsible for transporting and depositing the particles to the flat plate. If turbulence was the dominant factor contributing to enhanced particle deposition, then scaling by a turbulent parameter would make sense. The laminar impaction theory suggested that our range of Stk should not allow for deposition to occur on the impaction surface. However, by varying Stk from our results a substantial amount DF was measured. Given the lower range of Stk calculated and the large values of DF observed from these results, we concluded that deposition was enhanced by the turbulent motions in the wind tunnel. Furthermore, a

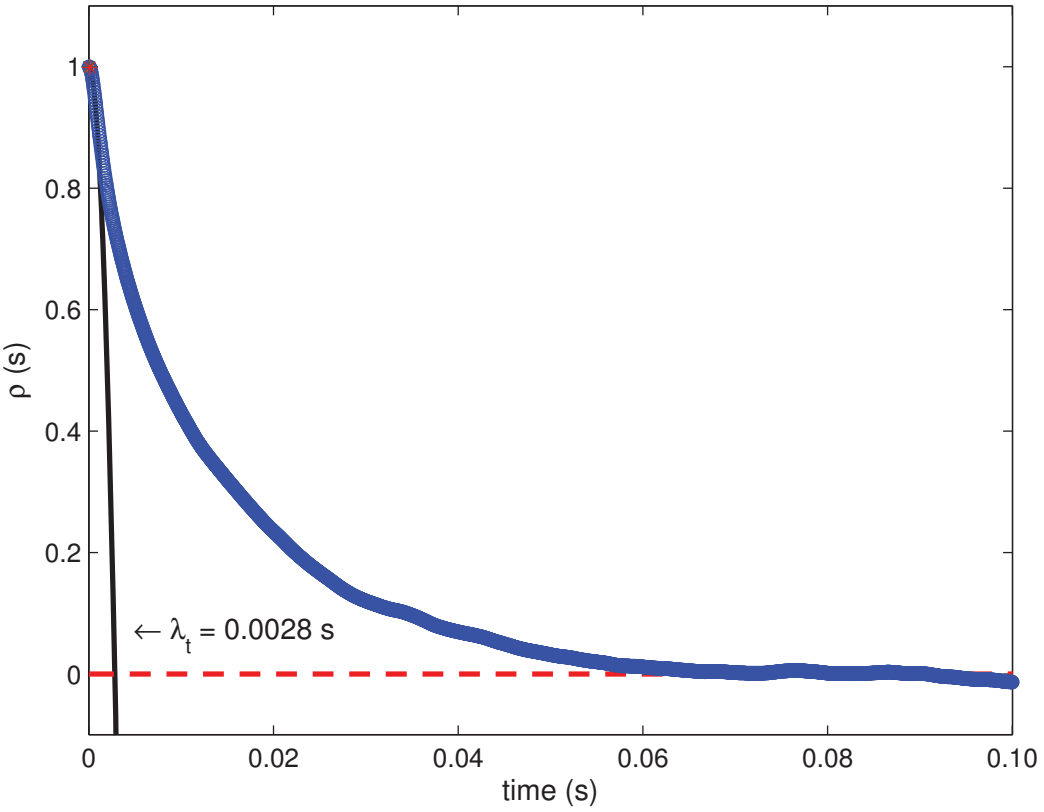

Figure B.10. Autocorrelation at U = 4.84 ms^{-1} and x = 2.13 m. The timescale of the Taylor microscale (λ_t) was determined by where the parabola crosses the x axis.

benchmark experiment between grid and no grid turbulence was performed which resulted in twice as much deposition on the impaction surface in the presence of a grid.

Enhancement of particulate deposition calculated from our results could be scaled by $R_\lambda{}^{0.3}$ to fit with the data from Marple and Liu [1]. These scaled results, fit to exact numerical solutions for laminar deposition, offered an empirical equation that could improve current and future deposition models which under-predict deposition due to the absent dynamics of the turbulent eddies. The contribution of the turbulent fluctuations u' and its associated turbulent lengthscale λ have been shown to be important parameters in turbulent deposition. Both u' and λ provide a framework to run future experiments and give a physical interpretation of the modified turbulent impaction parameter (DF_λ).

Once λ and u' were calculated for all velocities and locations, DF and the related Stk was scaled by R_λ^n. To determine the best fit exponent (n) to scale with R_λ, raw DF vs Stk data shown in Fig. 2.2 were fit to the theoretical curve of Marple and Liu [1] using a least squares minimization technique. First, Stk was scaled by R_λ^n using an appropriate range of n values (0.28-0.32). Then, the deposition fraction from Marple and Liu (DF_M) was found by interpolating between the higher and lower values of deposition fraction (DF_{M2} and DF_{M1}), as well as the Stokes number from Marple and Liu (Stk_{M2} and Stk_{M1}). This was necessary because our experimental values were not exactly the same as the theoretical values from Marple and Liu. The calculation of DF_M is shown in Eq. B.9:

$$DF_M = \left(\frac{DF_{M2} - DF_{M1}}{Stk_{M2} - Stk_{M1}}\right) \cdot (StkR_\lambda^n - Stk_{M2}) + DF_{M2}. \tag{B.9}$$

To compute the minimum error, the difference in deposition fraction between our scaled results (DF) and those of Marple and Liu (DF_M) was then squared for every data point and summed over all points. Where the sum of the errors had reached a local minimum was the best fit n value for scaling by R_λ^n. Shown in Fig. B.11, the best fit n value was 0.295 (rounded to 0.3 for results).

The modified impaction parameter for deposition (DF_λ) was shown in Ch.2 where DF_λ = 100-100/(440.5$(Stk^\star)^{3.88}$+1). Development of this empirical equation was essential in order to use known parameters (i.e., u' and λ) of the turbulent motions to improve deposition models where turbulence is present. This equation was also developed from a least squares fit starting from Eq. B.10:

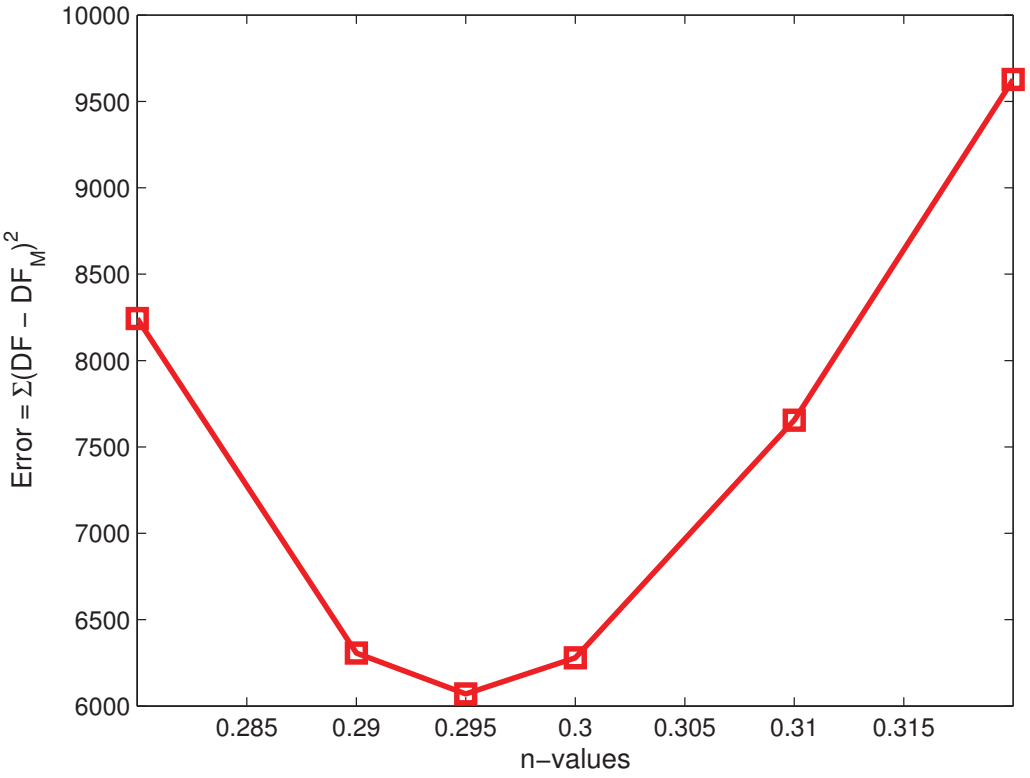

Figure B.11. A least squares minimization technique was used to fit our data closest to Marple and Liu [1]. An n of 0.295 best fit our data to the exact numerical solutions. For this paper n was rounded to be 0.3.

$$DF = 100 - \frac{100}{B(StkR_{\lambda}^{0.3})^{m} + 1}. \tag{B.10}$$

Manipulation of Eq. B.10 yielded a linear regression equation,

$$ln\left(\frac{100}{100 - DF} - 1\right) = ln(B) + m \cdot ln(StkR\lambda^{0.3}). \tag{B.11}$$

which was then plotted as ln[(100/(100-DF))-1] vs ln($Stk\mathrm{R}_{\lambda}{}^{0.3}$) in Fig. B.12. The linear equation developed from this regression analysis produced a slope m = 3.883 and a y intercept ln(B) of 6.088, so that B = 440.5. These values of B and m were input into Eq. B.10 and created the empirical equation (Eq. (2.3) for turbulent deposition where impaction was the dominant deposition mechanism.

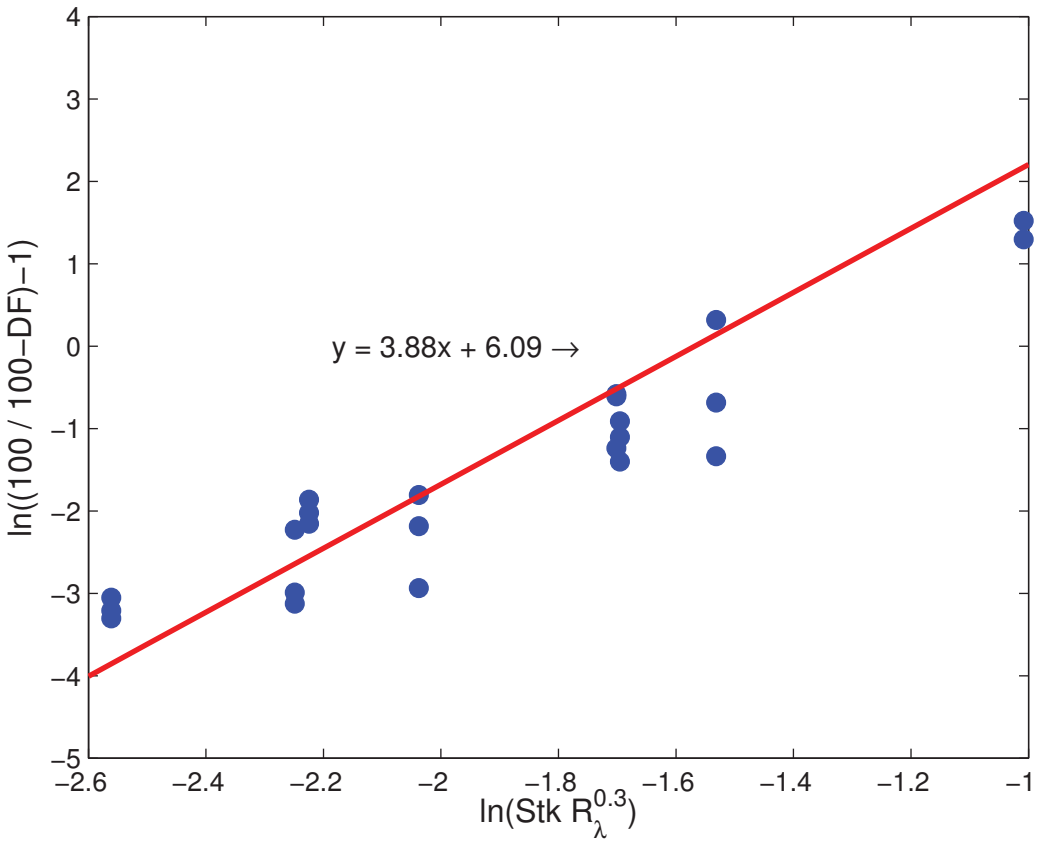

Figure B.12. A least squares curve fit was used to develop an empirical equation turbulent deposition where impaction is the dominant deposition mechanism. This fit yielded a new parameter to estimate DF given in Eq. 2.3.

REFERENCES

[1] V. Marple and B. Liu, "Characteristics of laminar jet impactors," *Env. Sci. Tech.*, vol. 8, pp. 648–654, 1974.

[2] "Unpaved roads section 13.2," Tech. Rep. AP 42, 2006.

[3] G. Muleski, C. Cowherd, and J. Kinsey, "Particulate emissions from construction activities," *Air and Waste Management Association*, vol. 55, pp. 772–783, 2005.

[4] J. Watson and J. Chow, "Reconciling urban fugitive dust emissions inventory and ambient source contribution estimates: Summary of current knowledge and needed research," Desert Research Institute, 2215 Raggio Parkway, Reno, NV 89512, Workshop Document 6110.4F, May 2000.

[5] E. Pardyjak, S. Speckart, F. Yin, and J. Veranth, "Near source deposition of vehicle generated fugitive dust on vegetation and buildings: model development and theory," *Atmos. Environ.*, vol. 42, pp. 6442–6452, 2008.

[6] T. Pace, "Methodology to estimate the transportable fraction (tf) of fugitive dust emissions for regional and urban scale air quality analyses," USEPA, Tech. Rep., 2005.

[7] C. Pope and D. Dockery, "Health effects of fine particulate air pollution: Lines that connect," *J. Air and Wast Mange. Assoc.*, vol. 56, pp. 709–742, 2006.

[8] J. Watson and J. Chow, "Clear sky visibility as a challenge for society," *Annual Review of Energy and Environment*, vol. 19, pp. 241–266, 1994.

[9] K. May and R. Clifford, "The impaction of aerosol particles on cylinders, spheres, ribbons and discs," *Ann. Occup. Hyg*, vol. 10, pp. 83–95, 1967.

[10] V. Etyemezian, "Field testing and evaluation of dust deposition and removal mechanisms - final report," Desert Research Institute, Reno, NV, Tech. Rep., January 2003.

[11] V. Etyemezian, J. Gillies, D. Gillette, and J. Veranth, "Deposition and removal of fugitive dust in the arid southwestern United States: measurements and model results," *Air and Waste Management Association*, vol. 54, pp. 1099–1111, 2004.

[12] J. Veranth, E. Pardyjak, and G. Seshadri, "Vehicle-generated dust transport: analytic models and field study," *Atmos. Environ.*, vol. 37, pp. 2295–2303, 2003.

[13] E. Pardyjak, P. Ramamurthy, and S. Speckart, "Development of windbreaks as a dust control strategy for communities in arid climates such as the US-Mexico border region," SCERP, Tech. Rep. A-04-06, 2007.

[14] J. Veranth, S. Speckart, V. Etyemezian, and E. Pardyjak, "Near-source deposition of vehicle-generated fugitive dust on vegetation and buildings," 2009, (unpublished).

[15] T. Ucar and F. Hall, "Windbreaks as a pesticide drift mitigation strategy: a review," *Pest Manag. Sci.*, vol. 57, pp. 663–675, 2001.

[16] W. Slinn, "Predictions for particle deposition to vegetative canopies," *Atmos. Environ.*, vol. 7, pp. 1785–1794, 1982.

[17] D. Aylor and T. Flesch, "Estimating spore release rates using a lagrangian stochastic simulation model," *J. Appl. Meteor.*, vol. 40, pp. 1196–1208, 2001.

[18] M. Raupach, N. Woods, G. Dorr, J. Leys, and H. Cleugh, "Entrapment of particles by windbreaks," *Atmos. Environ.*, vol. 35, pp. 3373–3383, 2000.

[19] D. Fryrear and E. Skidmore, "Methods of controlling wind erosion," *Soil Erosion and Crop Productivity*, pp. 443–457, 1985.

[20] K. Pell, L. Minsk, and K. Smith, "Snow fence guide," Strategic Highway Research Program, Washington, DC, SHRP-W/FR-91-106, 1991.

[21] B. Bailey, J. Stoll, and E. Pardyjak, "Dispersion in sparse agricultural canopies," (unpublished).

[22] S. Wilson, Y. Edgar, E. Matida, and M. Johnson, "Aerosol deposition measurements as a function of reynolds number for turbulent flow in a ninety-degree pipe bend," *Aerosol Science and Technology*, vol. 45, pp. 364–375, 2011.

[23] E. Matida, K. Nishino, and K. Torri, "Statistical simulation of particle deposition on the wall from turbulent dispersed pipe flow," *Int. J. Heat and Fluid Flow*, vol. 21, pp. 389–402, 2000.

[24] B. Grgic, W. Finlay, P. Burnell, and A. Heenan, "In vitro intersubject and intrasubject deposition measurements in realistic mouth-throat geometries," *J. Aerosol Science*, vol. 35, pp. 1025–1040, 2004.

[25] A. Lai, M. Byrne, and A. Goddard, "Aerosol deposition in turbulent channel flow on a regular array of three-dimensional roughness elements," *J. Aerosol Science*, vol. 32, pp. 121–137, 2001.

[26] G. Katul, T. Gronholm, L. S., and T. Vesala, "Predicting the dry deposition of aerosol-sized particles using layer-resolved canopy and pipe flow analogy models: role of turbophoresis." *J. Geophys. Res.*, vol. 115, pp. D12 202,doi:10.1029/2009JD012 853, 2010.

[27] J. Seinfeld and S. Pandis, *Atmospheric Chemistry and Physics*, 2nd ed. New York: Wiley-Interscience, 2006, vol. 1, ch. 19, pp. 902–906.

[28] D. Bache, "Analysing particulate deposition to plant canopies," *Atmos. Environ.*, vol. 15, pp. 1759–1761, 1981.

[29] L. Mydlarski and Z. Warhaft, "On the onset of high-reynolds-number grid-generated wind tunnel turbulence," *J. Fluid Mech*, vol. 320, pp. 331–368, 1996.

[30] G. Comte-Bellot and S. Corrsin, "The use of a contraction to improve the isotropy of grid-generated turbulence," *J. Fluid Mech*, vol. 25, pp. 657–682, 1966.

[31] S. Pope, *Turbulent Flows*, 1st ed. New York: Cambridge University Press, 2000, vol. 1, ch. 6, pp. 198–200.

[32] H. Tennekes and J. Lumley, *A First Course in Turbulence*, 1st ed. Massachusetts: The MIT Press, 1972, vol. 1, ch. 3, pp. 66–74.

[33] C. Cowherd, G. Muleski, and D. Gebhart, "Reinventing inventories – new ideas in New Orleans," New Orleans, LA, May 15–18," *Proceedings of the 15th international emission inventory conference*, 2006.

[34] A. Chamberlain, "Transport of lycopodium spores and other small particles to rough surfaces," *Proc. R. Soc*, vol. 296, pp. 45–70, 1967.

[35] S. Moran, E. Pardyjak, and J. Veranth, Eds., *Developing strategies for fugitive dust mitigation and transport flux using native vegetative windbreaks for dust control.*, ser. Proceedings of the 104th annual conference and exhibition. Orlando, FL: Air and Waste Management Association, 2011.

[36] H. Bruun, *Hot-Wire Anemometry: Principles and Signal Analysis*, 1st ed. New York: Oxford University Press, 1995, vol. 1, ch. 4, pp. 98–105.

[37] R. Wiener, K. Okazaki, and K. Willeke, "Influence of turbulence on aerosol sampling efficiency," *Atmos. Environ.*, vol. 22, pp. 917–928, 2001.

[38] T. Beckwith, R. Marangoni, and J. Lienhard, *Mechanical Measurements*, 6th ed. Upper Saddle River, New Jersey: Pearson Prentice Hall, 2007, ch. 3, pp. 73–80.

[39] R. Cionco, "Mathematical model for air flow in vegetative canopy," *J. Appl. Meteor.*, vol. 4, pp. 517–522, 1965.

[40] M. Judd, M. Raupach, and J. Finnigan, "A wind tunnel study of turbulent flow around single and multiple windbreaks, part 1: velocity fields," *Boundary-Layer Meteorology*, vol. 80, pp. 127–165, 1996.

[41] U. Amatul, "Implementation and validation of particle transport model for vegetation in quick urban dispersion modeling system," *MS Thesis, University of Utah*, 2006.

[42] W. Hinds, *Aerosol Technology: Properties, Behavior, and Measurement of Airborne Particles*, 2nd ed. New York: Wiley-Interscience, 1982, vol. 1, ch. 5, pp. 113–119.